Computer Methods in Applied Mechanics and Engineering 446 (2025) 118168

Contents lists available at ScienceDirect

Comput. Methods Appl. Mech. Engrg.

journal homepage: www.elsevier.com/locate/cma

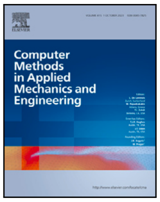

# The Stress-Continuous Material Point Method: A technique to alleviate cell-crossing instability while retaining linear shape functions

Giuliano Pretti, Robert E. Bird, William M. Coombs, Charles E. Augarde *, Stefano Giani

*Department of Engineering, Durham University, South Road, Durham, DH1 3LE, County Durham, UK*

## GRAPHICAL ABSTRACT

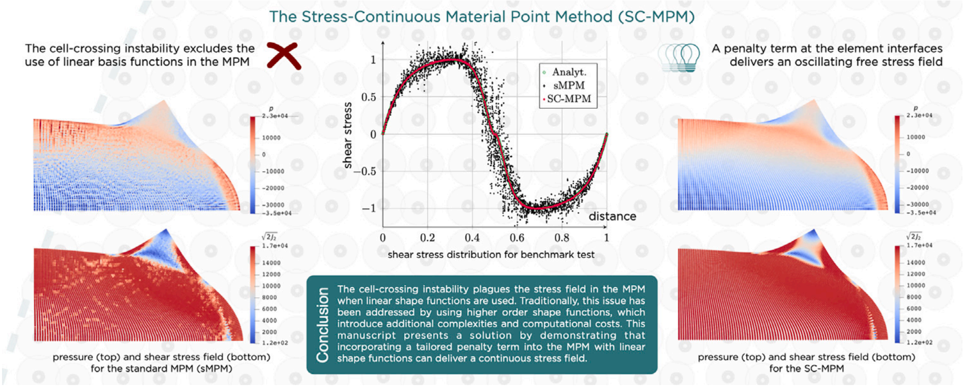

The Stress-Continuous Material Point Method (SC-MPM)

The cell-crossing instability excludes the use of linear basis functions in the MPM

A penalty term at the element interfaces delivers an oscillating free stress field

pressure (top) and shear stress field (bottom) for the standard MPM (sMPM)

shear stress distribution for benchmark test

The cell-crossing instability plagues the stress field in the MPM when linear shape functions are used. Traditionally, this issue has been addressed by using higher order shape functions, which introduce additional complexities and computational costs. This manuscript presents a solution by demonstrating that incorporating a tailored penalty term into the MPM with linear shape functions can deliver a continuous stress field.

pressure (top) and shear stress field (bottom) for the SC-MPM

## ARTICLE INFO

Dataset link: http://doi.org/10.15128/r17h149p91f

*Keywords:*
Material point method
Cell-crossing instability
Low-order shape functions
Implicit quasi-static
Finite strain elasto-plasticity

## ABSTRACT

The Material Point Method (MPM) for solid mechanics continues to attract much interest from those wishing to solve complex non-linear mechanics problems which include large deformations. Its prominence is rising in many areas of engineering, such as geotechnics and computer graphics due to the advantages it delivers over competitor methods. In the original MPM, the background grid is comprised of the simplest linear shape functions. These have the advantage of simplicity but also are the cause of a major defect that has been studied for a number of years, the cell-crossing instability. This manifests itself as unphysical oscillations in the stress fields predicted by the MPM and its cause is precisely the simplicity of the grid shape functions. The natural answer would seem to be to use higher order shape functions, but these functions are more challenging than the linear ones in other key aspects. In this paper we present a new MPM, the Stress-Continuous MPM, that maintains the simplicity of the original MPM by using the simplest elements, but alleviates the cell-crossing instability by employing a

---

* Corresponding author.
*E-mail address:* charles.augarde@durham.ac.uk (C.E. Augarde).

https://doi.org/10.1016/j.cma.2025.118168
Received 17 February 2025; Received in revised form 23 May 2025; Accepted 15 June 2025

novel penalty approach applied to element boundaries. The method has similarities and links to other stability measures developed for the MPM and used much more widely by researchers in the unfitted FEM community; these are explored in this paper. The new MPM is robustly tested on a number of numerical examples which show it to deliver an MPM formulation with linear shape functions and without severe cell-crossing issues.

## 1. Introduction

In the context of large deformation mechanics, the Material Point Method (MPM) [1,2] has gained popularity in accurately modelling history-dependent solid materials. The applications of the MPM span various fields of engineering, including the behaviour of soil [3] and soft materials [4], growth mechanics [5], and computer graphics [6], testifying to its versatility and reliability.

Despite this widespread use, the MPM still faces intrinsic challenges that reduce its reliability and ease of use. These mainly stem from the coexistence of a point-based discretisation (the Material Points, MPs), for storing the variables of interest for the simulation (e.g., density, stress), and a Finite Element grid, where the non-linear problem is solved incrementally. Despite its appearance, the method uses Lagrangian mechanics since the MPs move in a conforming way with the grid. However, the relative position of the points within the grid changes because the grid is discharged after the solution is reached and reintroduced before the new step. This decoupling of the MPs (which are also traditionally used as quadrature points) from the grid constitutes both the strength and the vulnerability of the MPM: on the one hand, grid distortion is less of a concern in the MPM, as there is only partial distortion during the increment before the grid is replaced. On the other hand, the lack of conformity between the grid and the MP-based discretisation undermines many certainties that underpin Finite Element Methods (FEMs).

One of the immediate consequences of decoupling the quadrature points from the grid is that linear shape functions cannot be used in the MPM without direct consequences. Since the original paper on the MPM employed these shape functions [1], this is often referred to as the standard MPM (sMPM) to distinguish it from formulations with different functions. Specifically, the sMPM is severely compromised by the so-called *cell-crossing instability*, which presents itself as a spurious oscillation in the stress field. The source of the cell-crossing instability lies in the discontinuity of the gradients of the linear shape functions at the junction between two adjacent elements. MPs moving across this discontinuity trigger this instability.

Traditionally, the cell-crossing instability is mitigated by increasing the continuity of the shape functions at these locations, as in Generalised Interpolation MPM (GIMPM) [7] or B-spline-based formulations [8], for example. To extend the continuity of the shape functions between two elements, larger stencils, positively-defined over at least three elements in a row, are required. However, the use of higher order shape functions with bigger stencils presents other challenges, which are discussed below. Any MPM formulation employing the MPs as integration points introduces a quadrature error arising from the incorrect position of the quadrature points (the MPs move accordingly to the solution field) and their weights, which are taken as proportional to the volume of the continuum ascribed to each MP.[1] However, as the order of the shape functions increases, the number of quadrature points required to minimise the integration error also rises, which, in turn, requires further treatment (see, e.g., [11]).

The quadrature error can also be exacerbated at the boundary of the problem domain, where small overlaps between the MPs' physical domains and grid elements may occur. This problem is referred to in the literature as the *small-cut* issue and leads to ill-conditioned linear systems. When higher order shape functions are used, this problem can affect multiple active boundary elements in a row, which themselves may not contain MPs, resulting in very small contributions to the entries of the linear system matrix.[2] The techniques designed to resolve the small-cut issue share the same underlying rationale, i.e., to control the solution at the nodal Degrees of Freedom (DoFs) suffering from the small-cut issue.[3]

Further problems arise with boundaries when using higher order shape functions in the MPM. If these functions are not modified to compact their stencil, they tend to blur the surface of the boundaries further, diffusing the boundaries over multiple elements. It follows that treating boundary conditions (BCs) [14,20–27] or phenomena involving the body's boundary (e.g., contact between solid bodies [28–30]) requires an *ad hoc* treatment.

However, if the stencils extend only over one element, conforming Dirichlet BCs can still be enforced on the grid without further treatments. Other shortcomings of larger stencils are that the MP-to-element search is more computationally expensive, and they have a less straightforward adaptation to simplex elements (i.e., triangles and tetrahedra), and, more generally, to unstructured grids.[4] On top of the above motivations, the GIMPM faces an extra layer of uncertainty regarding how and whether updating its

---

[1] A few techniques available in the literature have tried to alleviate the integration issue either by changing the quadrature rule and reconstructing historical variables, e.g., [9] or by modifying the MPs' weights or positions, e.g., [10].

[2] A discussion on how higher order shape functions exacerbate the small-cut issue in the MPM can be found in [12] (see Fig. 6B) for solid mechanics and in [13] for poro-mechanics (see Fig. 8). Both studies highlight that a higher condition number of the matrices to be inverted in the Newton–Raphson process is indicative of small-cut instabilities. Specifically, it is demonstrated that shape functions with larger stencils (e.g., the GIMPM) have a condition number that is considerably greater than that of their lower-order counterparts. For the same reason, the B-spline-based formulation proposed in [14] required a specific technique to address this instability.

[3] Amongst the techniques to counteract the small-cut issue, the *ghost method* [12,15], the *Extended B-splines method* [14,16,17] and the *aggregation* [18,19] have been introduced for the unfitted FEM and expanded more recently to the MPM.

[4] To the best of the authors' knowledge, only a few exception (see [31–36]) in the vast literature of MPM formulations have focused on unstructured grids.

characteristic domain should be undertaken. The literature does not provide a consensus on this (refer to [37] for a comparison of different domain update procedures).

It is clear from the above that there are clear advantages in using linear shape functions over their higher order counterparts linked to integration (within the bulk of the material and at the boundaries for the small-cut issue), boundary representations, performance of the MP-to-element assignment, and ease of application to simplex elements and unstructured grids. Therefore, one returns to examine ways to address the cell-crossing instability.

This paper presents a different perspective on the cell-crossing issue and provides a novel solution to permit the safe use of linear shape functions in the MPM. Instead of increasing the continuity of the shape functions, a tailored penalty term can be added to the classical MPM formulation which counteracts the unstable components that cause cell-crossing. Owing to its final purpose of delivering oscillation-free stress fields, the new method is named the *Stress-Continuous MPM* (SC-MPM). On top of retaining the above-listed advantages of linear shape functions with no significant cell-crossing, the discrete linear systems obtained with the SC-MPM are also well-conditioned and do not suffer from the small-cut issue. Additionally, the SC-MPM has the potential to straightforwardly transform an unfitted FEM code with low-order shape functions into a ready-to-use MPM code in a few steps.

The organisation of this manuscript is as follows: after this introduction, the equations for a solid material undergoing finite elasto-plastic deformations are outlined in Section 2 and discretised within an MPM environment in Section 3. The cell-crossing instability is dissected in Section 4, which motivates the introduction of the SC-MPM in Section 5, containing the key contributions of the manuscript. Numerical examples that support the SC-MPM and comparisons with other MPM formulations are presented in Section 6. Section 7 analyses the advantages and disadvantages of the SC-MPM over the competitor techniques.

## 2. Continuum and semi-discrete frameworks

This section introduces the components of non-linear solid mechanics which constitute the basis for the considered MPM formulation.

### *2.1. Governing equations*

#### *2.1.1. Kinematics and strain measures*

Let the body $\mathcal{B}$ in the reference configuration occupy a domain $\Omega$, which is a subspace of the Euclidean space $\mathcal{E}$ in $\mathbb{R}^{n^{dim}}$. Let this body be deformed according to the smooth mapping $\varphi : (\Omega, t) \to \omega \subset \mathcal{E}$, with $\omega$ being the domain of the current configuration at the generic time $t$. Let the Cartesian coordinates on $\Omega$ and $\omega$ be defined by the basis vectors $\boldsymbol{E}_I$ and $\boldsymbol{e}_i$, with $I, i = 1 \ldots n^{dim}$. For simplicity, this work assumes $\boldsymbol{E}_I = \boldsymbol{e}_i$. If $\boldsymbol{X}$ denotes the initial position of a point belonging to the body in $\Omega$, the mapping $\varphi$ describes the position of the same point in the current configuration, i.e., $x_i = \varphi_i\left(X_I, t\right)$ in $\omega$. The difference between these two positions, i.e., the current and the original one, is the displacement associated with the point originally in $\boldsymbol{X}$, i.e., $\boldsymbol{u} := \boldsymbol{x} - \boldsymbol{X}$. Let the deformation gradient $\boldsymbol{F}$ be the derivative of the mapping $\varphi$, whose components are given by

$$F_{iI}(\boldsymbol{X}) = \frac{\partial \varphi_i(\boldsymbol{X})}{\partial X_I}. \tag{1}$$

Based on the deformation gradient, this work employs the following measures of strain: the left Cauchy–Green strain $\boldsymbol{B} := \boldsymbol{F} \cdot \boldsymbol{F}^T$ (with $\cdot$ being the inner product, and $(\bullet)^T$ the transpose of $(\bullet)$), and the logarithmic strain $\boldsymbol{\epsilon} := \frac{1}{2} \ln \boldsymbol{B}$. The Jacobian, or volume ratio $J$, is given by the square root of the determinant of $\boldsymbol{B}$, i.e., $J := \sqrt{\det(\boldsymbol{B})}$. If $\mathrm{d}^0 v$ denotes an initial infinitesimal volume and $\mathrm{d}v$ its current counterpart, the Jacobian relates these measures of volume, i.e., $\mathrm{d}v = J\, \mathrm{d}^0 v$. Given the principle of mass conservation, the Jacobian also relates the initial and the current densities (${}^0\rho$ and $\rho$, respectively), according to the formula $\rho = \dfrac{{}^0\rho}{J}$.

As proposed by Kröner [38], Lee [39] and Mandel [40], this work assumes a multiplicative decomposition of the deformation gradient into elastic $\boldsymbol{F}^e$ and a plastic $\boldsymbol{F}^p$ parts, i.e., $\boldsymbol{F} = \boldsymbol{F}^e \cdot \boldsymbol{F}^p$. More generally, the superscripts $(\bullet)^e$ and $(\bullet)^p$ determine quantities whose definitions are based on the elastic and plastic parts of the deformation gradient, e.g., $\boldsymbol{B}^e := \boldsymbol{F}^e \cdot (\boldsymbol{F}^e)^T$.

#### *2.1.2. Balance of rate of linear momentum*

If inertia effects are neglected, the strong updated Lagrangian version of the balance of rate of linear momentum is given by

$$\mathbf{div} \cdot \boldsymbol{\sigma} + \rho\, \boldsymbol{b} = \mathbf{0} \quad \text{on } \omega, \tag{2}$$

where $\mathbf{div}$ denotes the divergence (i.e., $(\mathbf{div} \cdot \boldsymbol{\sigma})_i = \dfrac{\partial \sigma_{ij}}{\partial x_j}$) of the (symmetric) Cauchy stress $\boldsymbol{\sigma}$, while the body forces per unit mass are indicated by $\boldsymbol{b}$.

#### *2.1.3. Constitutive behaviour*

The free energy function $\Psi$ per unit initial volume under consideration is that of an isotropic Hencky material [41] and is given by

$$\Psi(\boldsymbol{\epsilon}, \boldsymbol{\alpha}) = \frac{K}{2}\left(\epsilon_v^e\right)^2 + \frac{3}{2} G \left(\epsilon_q^e\right)^2 + \tilde{\Psi}(\boldsymbol{\alpha}), \tag{3}$$

where $K > 0$ and $G > 0$ are the bulk and the shear moduli, while $\epsilon_v$ and $\epsilon_q$ are invariants of the logarithmic strain measure, defined by

$$\epsilon_v := \boldsymbol{\epsilon} : \mathbf{1}; \qquad \boldsymbol{e} := \boldsymbol{\epsilon} - \frac{\epsilon_v}{3}\mathbf{1}; \qquad \epsilon_q := \sqrt{\frac{2}{3}\,\boldsymbol{e} : \boldsymbol{e}}, \tag{4}$$

with $:$ being the double contraction operator between tensors, and $\mathbf{1}$ the second order identity tensor. In Eq. (3), $\tilde{\Psi}$ defines a part of the free energy function responsible for the isotropic hardening, based on a set of internal variables $\boldsymbol{\alpha}$.

Following the Coleman-Noll procedure [42,43], the elastic constitutive behaviour of the material can be decoupled from the dissipation, leading to

$$\boldsymbol{\tau} = 2\,\frac{\partial \Psi}{\partial \boldsymbol{B}^e} \cdot \boldsymbol{B}^e; \qquad \boldsymbol{q} = -\frac{\partial \tilde{\Psi}}{\partial \boldsymbol{\alpha}}, \tag{5}$$

where $\boldsymbol{\tau} = J\,\boldsymbol{\sigma}$ is the Kirchhoff stress and $\boldsymbol{q}$ are the thermodynamic forces. For the isotropic plastic part, this work considers the principle of maximum dissipation (see [44,45]), which results in the flow rule and the evolution of the internal variables

$$\boldsymbol{d}^p = \dot{\gamma}^p \frac{\partial \Phi(\boldsymbol{\tau}, \boldsymbol{q})}{\partial \boldsymbol{\tau}}; \qquad \dot{\boldsymbol{\alpha}} = \dot{\gamma}^p \frac{\partial \Phi(\boldsymbol{\tau}, \boldsymbol{q})}{\partial \boldsymbol{q}}, \tag{6}$$

where $\boldsymbol{d}^p := \operatorname{sym}\big(\boldsymbol{F}^e \cdot \dot{\boldsymbol{F}}^p \cdot (\boldsymbol{F}^p)^{-1} \cdot (\boldsymbol{F}^e)^{-1}\big)$ is the symmetric part of the plastic velocity gradient, $\Phi(\boldsymbol{\tau}, \boldsymbol{q})$ is the yield function, and $\dot{\gamma}^p$ is the plastic multiplier. The $(\dot{\bullet})$ notation expresses the material time derivative of $(\bullet)$. As explained in Simo [46,47], the above set of equations extends the small-strain additive decomposition for elasto-plasticity to the case of finite strains if exponential integration schemes are employed.

### 2.2. Boundary conditions

For the problem under consideration, it is assumed that Dirichlet and Neumann boundary conditions (BCs) are prescribed on the current boundaries $\partial\omega_D$ and $\partial\omega_N$, which satisfy $\partial\omega = \partial\omega_D \cup \partial\omega_N$ and $\partial\omega_D \cap \partial\omega_N = \emptyset$. Specifically, it is considered that

$$\boldsymbol{u} = \boldsymbol{u}_D \qquad \text{on } \partial\omega_D; \tag{7}$$

$$\boldsymbol{\sigma} \cdot \boldsymbol{n} = \mathbf{0} \qquad \text{on } \partial\omega_N, \tag{8}$$

where $\boldsymbol{n}$ indicates the outer normal. For simplicity and without loss of generality, this work assumes homogeneous Neumann boundary conditions. Readers interested in the application of inhomogeneous Neumann boundary conditions in the MPM may refer to [20–23] for further information.

### 2.3. Time-discrete, spatially continuous weak form

Since it is recognised that the constitutive equations are non-linear and path-dependent, the equations must be set in a incremental form. This motivates the introduction of a Backward-Euler (pseudo)-time discretisation between the current $n+1$ configuration and the previously converged one $n$. Dropping the subscript $(\bullet)_{n+1}$ for the quantities referred to the current configuration, the time-incremental displacement over the considered interval is denoted by $\Delta\boldsymbol{u} := \boldsymbol{u} - \boldsymbol{u}_n$. The space of trial functions is given by

$$\mathscr{V}_{\boldsymbol{u}_D}(\omega) = \left\{ \Delta\boldsymbol{u} \in \left(H^1(\omega)\right)^{n^{dim}} \;\middle|\; \Delta\boldsymbol{u} = \Delta\boldsymbol{u}_D \text{ on } \partial\omega_D \right\}, \tag{9}$$

where $H^1(\omega)$ indicates the Sobolev space of functions in $H^0(\omega)$ with weak gradients also in $H^0(\omega)$. A similar space, denoted by $\mathscr{V}_{\mathbf{0}}(\omega)$, is employed for the test functions $\delta\Delta\boldsymbol{u}$.

Hence, exploiting the calculus fundamental lemma and the divergence theorem for the BCs (8), the time-discrete and continuous in space weak form is as follows: given $\boldsymbol{\alpha}_n$ and $\boldsymbol{u}_n$, seek $\Delta\boldsymbol{u} \in \mathscr{V}_{\boldsymbol{u}_D}(\omega)$ such that

$$\int_\omega \mathbf{grad}\,\delta\Delta\boldsymbol{u} : \boldsymbol{\sigma}\left(\boldsymbol{\alpha}_n, \boldsymbol{u}\right)\,\mathrm{d}v - \int_\omega \delta\Delta\boldsymbol{u} \cdot \rho\,\boldsymbol{b}\,\mathrm{d}v = 0, \qquad \forall \delta\Delta\boldsymbol{u} \in \mathscr{V}_0(\omega). \tag{10}$$

To fully complete the discretisation process, discrete geometry and variables must also be introduced. These are addressed in the following section.

## 3. The material point method

This section introduces the MPM, defines the labels for the discrete parts of the geometry and introduces the discrete spaces of trial and test functions.

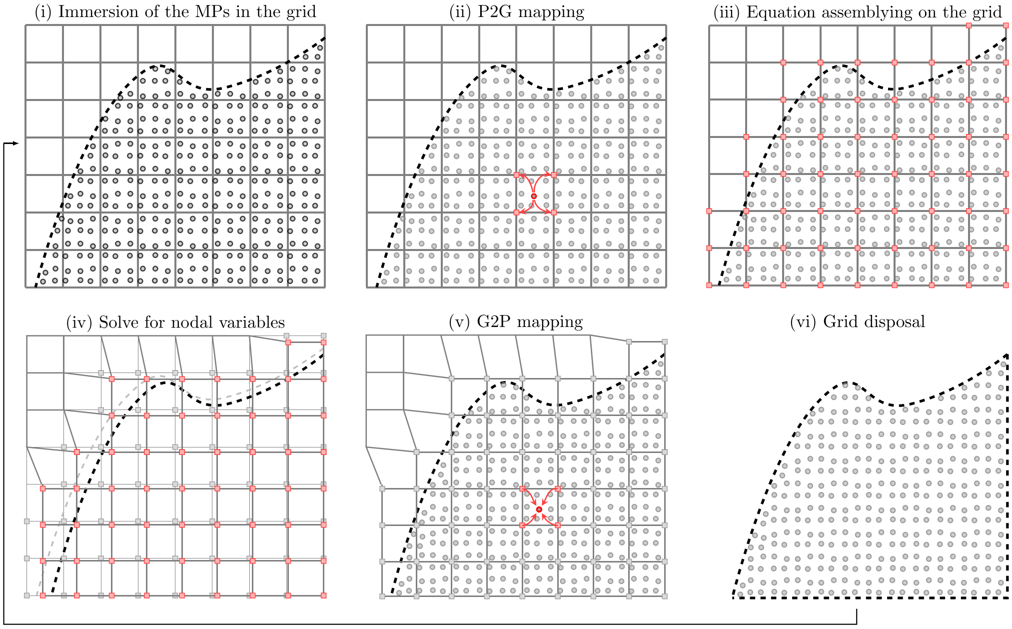

**Fig. 1.** MPM step phases. *Source*: Figure reproduced from Pretti et al. [13].

### 3.1. MPM algorithm

The MPM-based discretisation comprises a cloud of Material Points (MPs) representing the problem domain, where the MPs carry all the information (e.g., density, stress, etc.) necessary to run the analysis. At each increment, the MPs are immersed in a new regular grid, Phase (i) in Fig. 1. Since no information is stored at the grid nodes, a mapping from the MPs to the grid is necessary[5] to initialise the grid nodal values. This mapping is called Point-to-Grid (P2G) and is illustrated by Phase (ii) in Fig. 1. The equations are then assembled at the active grid nodes, employing the MPs as quadrature points, Phase (iii) in Fig. 1. Since the MPM is a Lagrangian method, the grid incremental solution deforms the grid and, conformingly, the MPs displace, Phase (iv) in Fig. 1. If, as here, the solution is obtained using an *implicit* approach, Phases (iii) and (iv) are iteratively repeated until a convergence criterion is met. Since the grid is employed only to compute the incremental solution, it is introduced anew at every time-step. Hence, it is necessary to map the updated solution from the grid nodes back to the MPs. This is the Grid-to-Point (G2P) mapping and is illustrated by Phase (v) in Fig. 1. Following the G2P mapping, the grid is discarded, Phase (vi) in Fig. 1. The introduction of a new computational grid marks the beginning of a new step and the above-described phases are repeated until the problem is solved completely.

### 3.2. Nomenclature of the computational domains and discretisations

Each point has a volume $v^{mp}$ and is representative of a portion of domain $\omega^{mp}$ such that $\omega \approx \omega^{MP} := \bigcup_{mp=1}^{N^{mp}} \omega^{mp}$, with $N^{mp}$ being the total number of MPs in the simulation (see Fig. 2(a)).

At every time-step, a finite element grid ${}^{h}\mathcal{T}$ is introduced, Fig. 2(b). This grid discretises a portion of the Euclidean space $\mathcal{E}$, which fully contains the MP-based discrete domain $\omega^{MP}$. The grid ${}^{h}\mathcal{T}$ consists of elements $K$ (see Fig. 2(b)) with representative grid size $h := \max_{K \in {}^{h}\mathcal{T}} h_K$. These elements acts as finite elements in the Finite Element Method, i.e., they possess a set of nodal variables and discretise a portion of the space over which shape functions are defined. However, for a given time-step, not all the elements are active.

Let the active elements of the grid be those for which all the nodal shape functions computed at an MP's current position $\boldsymbol{x}^{mp}$ gives a non-null contribution, i.e.,

$$ {}^{h}\mathcal{T}^{act} := \left\{ K \in {}^{h}\mathcal{T} \;\middle|\; \exists\, \boldsymbol{x}^{mp} : \mathrm{N}_{\mathsf{A}}\left(\boldsymbol{x}^{mp}\right) > 0 \; \forall \mathsf{A} \in \mathcal{N}\left(K\right) \right\}, \tag{11} $$

where $\mathcal{N}(K)$ indicates the set of nodes (vertices) belonging to the $K-$th element and $\mathrm{N}_{\mathsf{A}}$ are the elemental shape functions associated with the node $\mathsf{A} \in \mathcal{N}(K)$. It follows that the current active grid domain, i.e., ${}^{h}\hat{\omega} := \bigcup_{K \in {}^{h}\mathcal{T}^{act}} K$ encompasses the MPs' domains ${}^{h}\hat{\omega} \supseteq \omega^{MP}$.

---

[5] The initial mapping from the MPs to the grid is not always necessary in the MPM. For example, if a quasi-static irreducible, displacement-based formulation for solid mechanics is used, no mapping is required. For a more detailed discussion on this topic, see Pretti et al. [48].

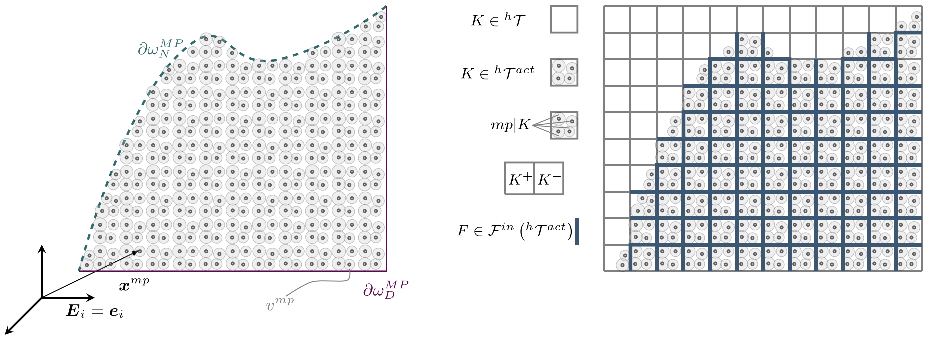

(a) MP-based discretisation for the MPM. Dirichlet (conforming) and Neumann (non-conforming) boundaries are highlighted. Positions and representative volumes of the MPs are visualised too.

(b) Grid-based discretisation for the MPM. A legend of the grid-related quantities is included too.

**Fig. 2.** Different discretisations in the MPM: the MP-based discretisation is represented on the left, while the grid-based discretisation is on the right.

For reasons that will be explained in Section 5, let $\mathcal{F}(K)$ denote the set of elemental facets[6] of a grid element $K$. If a single facet $F$ is the intersection $F = \partial K^+ \cap \partial K^-$ of two elements $K^+, K^- \in {}^h\mathcal{T}$, $F$ is an *interior* facet when shared between two active elements of $\mathcal{T}$ (i.e., if $K^+, K^- \in {}^h\mathcal{T}^{act}$). Let the set of all interior facets be denoted by $\mathcal{F}^{in}\left({}^h\mathcal{T}^{act}\right)$ (see, again, Fig. 2(b)) and $\gamma_F$ be the surface of each of these facts. For simplicity, let us assume that the MPs' Dirichlet boundary $\partial\omega_D^{MP}$ conforms to its grid counterpart throughout the simulation,[7] i.e, $\partial^h\hat{\omega}_D \approx \partial\omega_D^{MP}$ (see Fig. 2(a)). This assumption permits the strong imposition of the Dirichlet boundary conditions for shape function with compact stencil.

### 3.3. Discrete spaces and MPM weak form

In light of the MPM algorithm described in Section 3.1 and the discretisation nomenclature in Section 3.2, the discrete MPM formulation can now be provided. In the case of the sMPM, the space of linear polynomials over the active elements $K \in {}^h\mathcal{T}^{act}$ (denoted $\mathcal{P}^1(K)$), and the space of continuous functions over the active grid domain (labelled $C^0\left({}^h\hat{\omega}\right)$) are introduced. The space of trial functions for the sMPM is given by

$$ {}^h\mathscr{V}_{\boldsymbol{u}_D}\left({}^h\hat{\omega}\right) = \left\{ \Delta^h\boldsymbol{u} \in \left(C^0\left({}^h\hat{\omega}\right)\right)^{n^{dim}} \;\middle|\; \Delta^h\boldsymbol{u}|_K \in \left(\mathcal{P}^1(K)\right)^{n^{dim}},\ \Delta^h\boldsymbol{u}|_{\mathsf{A}} = \Delta\boldsymbol{u}_D\left(\boldsymbol{x}_{\mathsf{A}}\right)\ \forall\mathsf{A} \in \mathcal{N}\left(\partial^h\hat{\omega}_D\right) \right\}, \tag{12} $$

with $\Delta^h\boldsymbol{u}|_K$ (or $\Delta^h\boldsymbol{u}|_{\mathsf{A}}$) being the restriction of the trial function to the $K$−th element (or $\mathsf{A}$−th node) and $\mathcal{N}\left(\partial^h\hat{\omega}_D\right)$ the set of nodes belonging to the (conforming) Dirichlet boundary. A similar definition to the above follows for the test function $\delta\Delta^h\mathbf{u} \in {}^h\mathscr{V}_{\mathbf{0}}\left({}^h\hat{\omega}\right)$. Having introduced these spaces, the discrete weak form reads as follows: given $\boldsymbol{\alpha}_n$ and $\boldsymbol{u}_n$, find $\Delta^h\boldsymbol{u} \in {}^h\mathscr{V}_{\boldsymbol{u}_D}\left({}^h\hat{\omega}\right)$ s.t.

$$ \sum_K \left( \int_K \mathbf{grad}\,\delta\Delta^h\boldsymbol{u} : \boldsymbol{\sigma}\left(\boldsymbol{\alpha}_n, {}^h\boldsymbol{u}\right) \mathrm{d}v - \int_K \delta\Delta^h\boldsymbol{u}\cdot\rho\,\boldsymbol{b}\,\mathrm{d}v \right) = 0, \qquad \forall\delta\Delta^h\boldsymbol{u} \in {}^h\mathscr{V}_{\mathbf{0}}\left({}^h\hat{\omega}\right). \tag{13} $$

As no integration rule has been specified so far (and this work agrees with others in seeing the sMPM as a FEM with a relaxed integration scheme, see [49,50]), the above-introduced formulation matches that of a FEM if the conforming case in considered, i.e., if $\omega \approx {}^h\hat{\omega}$. If a non-conforming case is considered, i.e., $\omega \subset {}^h\hat{\omega}$, the above formulation is similar to that of an unfitted FEM and precautions must be taken to address the *small-cut* instability in the boundary regions (see Burman [15] or Coombs [12]). However, as will be explained in Section 5, one of the good aspects of the new formulation suggested in this work is that the small-cut issue is automatically taken care of.

If the MPs are taken as quadrature points whose weight is given by their volumes, the sMPM weak form becomes: given $\boldsymbol{\alpha}_n^{mp}$ and $\boldsymbol{u}_n^{mp}$, find $\Delta^h\boldsymbol{u} \in {}^h\mathscr{V}_{\boldsymbol{u}_D}\left({}^h\hat{\omega}\right)$ s.t.

$$ \sum_K \sum_{mp|K} \left( v^{mp}\left(\boldsymbol{u}^{mp}\right) \mathbf{grad}\,\delta\Delta^h\boldsymbol{u}\left(\boldsymbol{x}^{mp}\right) : \boldsymbol{\sigma}\left(\boldsymbol{\alpha}_n^{mp}, \boldsymbol{u}^{mp}\right) - m^{mp}\,\delta\Delta^h\boldsymbol{u}\left(\boldsymbol{x}^{mp}\right)\cdot\boldsymbol{b}\left(\boldsymbol{x}^{mp}\right) \right) = 0, \qquad \forall\delta\Delta^h\boldsymbol{u} \in {}^h\mathscr{V}_{\mathbf{0}}\left({}^h\hat{\omega}\right), \tag{14} $$

where the extended dependency of the current displacements at the MPs is as follows $\boldsymbol{u}^{mp}\left(\boldsymbol{u}_n^{mp}(\Delta^h\boldsymbol{u}_0, \ldots \Delta^h\boldsymbol{u}_n), \Delta^h\boldsymbol{u}\right)$, and $mp|K$ are the MPs that the elemental shape functions see, which depends on the shape functions' stencil. In the case of sMPM, the

---

[6] In the $n^{dim}$−th dimensional space, the term *facets* is employed to denote a face with dimension $n^{dim} - 1$, i.e., a point, an edge, and a face for $n^{dim} = 1, 2, 3$, respectively.

[7] As for the case of Neumann BCs, the application of non-conforming Dirichlet BCs in the MPM is not addressed in this manuscript. Interested readers can refer to [14,24–27].

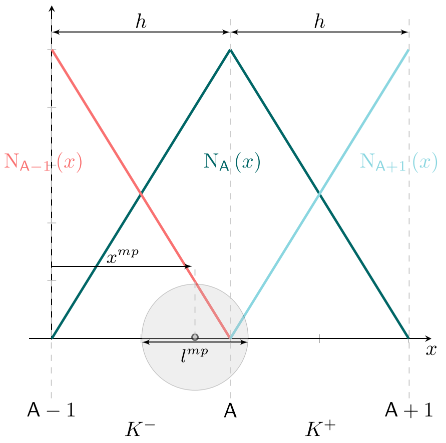

(a) Geometrical setup and linear shape functions on the considered domain $\hat{K}$.

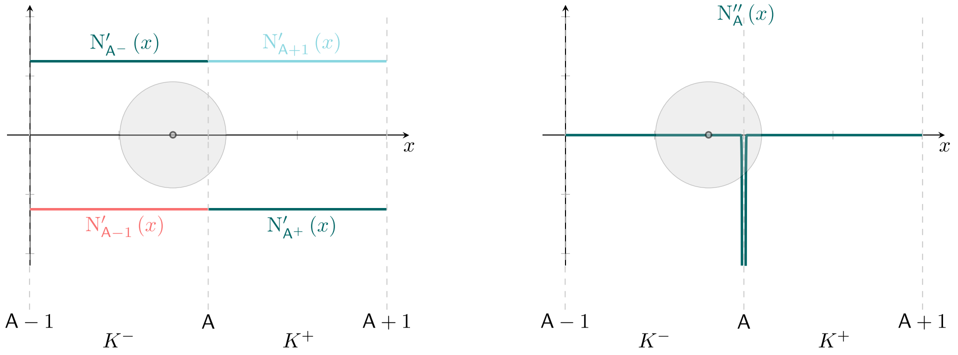

(b) Shape functions' first derivatives on $\hat{K}$.

(c) Shape functions' second derivatives on $\hat{K}$ (qualitative plot).

**Fig. 3.** Setup of $\hat{K}$ (top) with shape functions, first (bottom left) and second (bottom right) derivatives. The position of the ball $\mathcal{B}$ in proximity of the A−th node is also illustrated.

$mp|K$ coincides with the MPs in the $K$−th element. The mass of each material point is given by its density and its volume, i.e., $m^{mp} = \rho^{mp}\, v^{mp} = {}^0\rho^{mp}\, {}^0v^{mp}$.

In the numerical examples in Section 6, the results are sometimes compared with those coming from the Generalised Interpolation MPM (GIMPM) (see [7,51] for definition and details of implementations). In the GIMPM formulation, shape functions with higher regularity, specifically $C^1\left({}^h\hat{\omega}\right)$, are used, obtained via the convolution integral of the functions in ${}^h\mathscr{V}_{\boldsymbol{u}_D}\left({}^h\hat{\omega}\right)$ with a constant function centred at the MPs' location (the *characteristic* function). For the purpose of this work, the critical aspect is the greater regularity of these functions, which, however, occurs with a larger stencil and the issues already cited above. Similar conclusions on higher regularity and larger stencils can be drawn for B-Splines MPM, see, for instance, [8,52].

## 4. The cell-crossing instability

This section discusses the cell-crossing instability, which mainly affects the sMPM and sets the scene for the SC-MPM. Specifically, Section 4.1 presents a straightforward mono-dimensional setting that quantifies the cell-crossing instability and justifies the adoption of a penalty term in the SC-MPM (fully detailed in Section 5), while Section 4.2 provides a more mathematical explanation of the underlying problem.

### 4.1. Derivation of the penalty for the SC-MPM in a mono-dimensional case

This section considers the setting represented in Fig. 3. This setup is designed to quantify the cell-crossing instability by comparing the internal force vector calculated using the FEM with linear shape functions and that calculated using the sMPM. Both methods employ the same setup, and the transition from one method to the other will be clear based on the context. For this case and throughout this section, let us assume hypothesis of the small deformation ($\|\mathbf{grad}\,\boldsymbol{u} + (\mathbf{grad}\,\boldsymbol{u})^T\| \ll 1$, with $\|\bullet\|$ being the

Euclidean/Frobenius norm for vectors/tensors) with finite displacements ($\|\boldsymbol{u}\| \gg h\,\|\mathbf{grad}\,\boldsymbol{u} + (\mathbf{grad}\,\boldsymbol{u})^T\|$) and linear elastic material. The setup of Fig. 3 is mono-dimensional (i.e., $n^{dim} = 1$), so the Young's modulus $E$ fully characterises the material behaviour. For clarity of notation, it is specified that when general quantities are computed on the right-hand side (RHS) of the $\mathsf{A}$−th node, these are denoted by $(\bullet)^+$. Conversely, they are indicated by $(\bullet)^-$ when on the left-hand side (LHS) of the same node. Employing this style of notation, the setup in Fig. 3 also assumes that the grid is uniform: $h = h^+ = h^-$.

Let us consider the following integral of the internal force vector coming from the FEM employing linear shape functions over two neighbouring elements $\hat{K} = K^- \cup K^+$ (see Fig. 3(a))

$$\mathrm{f}_{\mathsf{A}}^{int,FEM}\Big|_{\hat{K}} := \int_0^{2h} \mathrm{N}'_{\mathsf{A}}(x) \underbrace{\sum_{\mathsf{B}} \mathrm{N}'_{\mathsf{B}}(x)\, E\, \mathrm{u}_{\mathsf{B}}}_{=\sigma(x)}\, \mathrm{d}x, \qquad \text{for } \mathsf{B} = \{\mathsf{A}-1, \mathsf{A}, \mathsf{A}+1\}. \tag{15}$$

The above integral can be partitioned into two parts: one relative to a bubble $\mathcal{B}$ centred at the position $x^{mp}$ and of diameter (or length, in this 1D setup) $l^{mp}$, and its complementary part $\hat{K} \setminus \mathcal{B}$ (i.e., the two neighbouring elements with the exclusion of the bubble domain). The partition of the integral of the FEM into these two parts is performed to exclude the difference between FEM and sMPM regarding how the integral volume is represented. This separation enables the focus to be on the spurious components related to the cell-crossing. Specifically, the considered bubble must intersect the two neighbouring elements to identify the unstable components coming from the cell-crossing. In light of this partition, the FEM internal force vector can be written as a function of the position of the centre of the bubble, i.e.,

$$\begin{aligned}\mathrm{f}_{\mathsf{A}}^{int,FEM}\Big|_{\hat{K}} &= \mathrm{f}_{\mathsf{A}}^{int,FEM}\Big|_{\mathcal{B}}(x^{mp}) + \mathrm{f}_{\mathsf{A}}^{int,FEM}\Big|_{\hat{K}\setminus\mathcal{B}}(x^{mp}) \\ &= \int_{x^{mp}-l^{mp}/2}^{x^{mp}+l^{mp}/2} \mathrm{N}'_{\mathsf{A}}(x) \sum_{\mathsf{B}} \mathrm{N}'_{\mathsf{B}}(x)\, E\, \mathrm{u}_{\mathsf{B}}\, \mathrm{d}x + \mathrm{f}_{\mathsf{A}}^{int,FEM}\Big|_{\hat{K}\setminus\mathcal{B}}(x^{mp}).\end{aligned} \tag{16}$$

Focusing on the integral on the bubble's domain, its integrand function can be approximated with a Taylor expansion at $x = x^{mp}$, which gives

$$\begin{aligned}\mathrm{f}_{\mathsf{A}}^{int,FEM}\Big|_{\mathcal{B}}(x^{mp}) = {}& \mathrm{N}'_{\mathsf{A}}(x^{mp}) \sum_{\mathsf{B}} \left(\mathrm{N}'_{\mathsf{B}}(x^{mp})\, E\, \mathrm{u}_{\mathsf{B}}\right) \int_{x^{mp}-l^{mp}/2}^{x^{mp}+l^{mp}/2} \mathrm{d}x \\ & \underbrace{+ E \sum_{\mathsf{B}} \left( \mathrm{u}_{\mathsf{B}} \int_{x^{mp}-l^{mp}/2}^{x^{mp}+l^{mp}/2} \left(\mathrm{N}'_{\mathsf{A}}(x)\, \mathrm{N}'_{\mathsf{B}}(x)\right)'\Big|_{x^{mp}} (x - x^{mp})\, \mathrm{d}x \right)}_{:=\mathrm{R}_{\mathsf{A}}^{(1)}(x^{mp})} + \sum_{q=2}^{\infty} \mathrm{R}_{\mathsf{A}}^{(q)}(x^{mp}),\end{aligned} \tag{17}$$

where $|\mathrm{R}_{\mathsf{A}}^{(q)}(x^{mp})| = \int_{x^{mp}-l^{mp}/2}^{x^{mp}+l^{mp}/2} \mathcal{O}\left((x - x^{mp})^q\right)\, \mathrm{d}x$ as $x \to x^{mp}$ and $\mathcal{O}$ indicates the leading order of the approximating terms. Since the diameter of the bubble has been chosen to have the same volume (or length, for this 1D example) that the MP represents, i.e. $\int_{x^{mp}-l^{mp}/2}^{x^{mp}+l^{mp}/2} \mathrm{d}x = l^{mp}$, it can be seen that the $0$−th term of the Taylor expansion is the internal force vector computed via the sMPM, i.e.,

$$\mathrm{f}_{\mathsf{A}}^{int,FEM}\Big|_{\mathcal{B}}(x^{mp}) = \mathrm{f}_{\mathsf{A}}^{int,sMPM}(x^{mp}) + E \sum_{\mathsf{B}} \left( \mathrm{u}_{\mathsf{B}} \int_{x^{mp}-l^{mp}/2}^{x^{mp}+l^{mp}/2} \left(\mathrm{N}'_{\mathsf{A}}(x)\, \mathrm{N}'_{\mathsf{B}}(x)\right)'\Big|_{x^{mp}} (x - x^{mp}) \right) \mathrm{d}x + \sum_{q=2}^{\infty} \mathrm{R}_{\mathsf{A}}^{(q)}(x^{mp}). \tag{18}$$

Hence, the above equation clarifies that the difference between the sMPM internal force vector due to a single MP and the internal force vector of the linear FEM over a bubble of the same length is an integration error which can be quantified by Taylor expansion terms of order bigger than zero. Let us now focus on the $1$−st term of the Taylor expansion, which gives

$$\mathrm{R}_{\mathsf{A}}^{(1)}(x^{mp}) = E \sum_{\mathsf{B}} \mathrm{u}_{\mathsf{B}} \left( \int_{x^{mp}-l^{mp}/2}^{x^{mp}+l^{mp}/2} \mathrm{N}''_{\mathsf{A}}(x^{mp})\, \mathrm{N}'_{\mathsf{B}}(x^{mp})\, (x - x^{mp})\, \mathrm{d}x + \int_{x^{mp}-l^{mp}/2}^{x^{mp}+l^{mp}/2} \mathrm{N}'_{\mathsf{A}}(x^{mp})\, \mathrm{N}''_{\mathsf{B}}(x^{mp})\, (x - x^{mp})\, \mathrm{d}x \right). \tag{19}$$

The derivatives of the linear shape functions under consideration $\mathrm{N}_{\mathsf{A}}(x) = 1 - \frac{1}{h}|x - x_{\mathsf{A}}|$ are given by (compare with Fig. 3(b))

$$\mathrm{N}'_{\mathsf{A}}(x) = -\frac{1}{h} \operatorname{sign}\left(x - x_{\mathsf{A}}\right). \tag{20}$$

The second derivatives of these functions can only be quantified in a distributional sense, i.e.,

$$\int_{\mathbb{R}} \mathrm{N}''_{\mathsf{A}}(x)\, g(x)\, \mathrm{d}x = -\int_{\mathbb{R}} \frac{2}{h} \delta_{x_{\mathsf{A}}}\, g(x)\, \mathrm{d}x = -\frac{2}{h} g\left(x_{\mathsf{A}}\right), \tag{21}$$

for a generic function $g(x)$ at least in $H^1(\mathbb{R})$, and with $\delta_{x_{\mathsf{A}}}$ being the Dirac distribution centred at the $\mathsf{A}$−th node. Hence, the integral of the second derivatives of the shape functions is non-zero only in the proximity of the $\mathsf{A}$−th node. This means that the term $\mathrm{R}_{\mathsf{A}}^{(1)}(x^{mp})$ is non-zero ***only*** when cell-crossing happens and that the contribution of the second term on the RHS of Eq. (19) is non-null only when $\mathsf{B} = \mathsf{A}$ (compare with Fig. 3(c)). Using a small positive quantity $\epsilon$ to still express the term $\mathrm{R}_{\mathsf{A}}^{(1)}(x^{mp})$ as an integral, it follows that

$$\mathrm{R}_{\mathsf{A}}^{(1)}(x^{mp}) = \lim_{\epsilon \to 0} \left( E \sum_{\mathsf{B}} \left( \mathrm{u}_{\mathsf{B}}\, \mathrm{N}'_{\mathsf{B}}(x^{mp}) \int_{-\epsilon + x_{\mathsf{A}}}^{x_{\mathsf{A}}+\epsilon} \mathrm{N}''_{\mathsf{A}}(x^{mp})(x - x^{mp})\, \mathrm{d}x \right) + E\, \mathrm{u}_{\mathsf{A}}(x^{mp})\, \mathrm{N}'_{\mathsf{A}}(x^{mp}) \int_{-\epsilon + x_{\mathsf{A}}}^{x_{\mathsf{A}}+\epsilon} \mathrm{N}''_{\mathsf{A}}(x - x^{mp})\, \mathrm{d}x \right). \tag{22}$$

Since in the MPM the position of the point at different time-steps can vary, and the point can be first on the left of the A−th node (for a given grid) and then later on its right (for the new grid at the start of next step), $x^{mp}$ is a variable. The notations $\mathrm{B}^- = \{\mathrm{A}-1, \mathrm{A}^-\}$ and $\mathrm{B}^+ = \{\mathrm{A}^+, \mathrm{A}+1\}$ are then useful to distinguish further which side of the first derivatives are under consideration. To remove the ambiguity of the sign functions appearing in these functions (see Eq. (20) and Fig. 3(b)), the above integrals can be written as

$$\begin{aligned}\mathrm{R}_{\mathrm{A}}^{(1)}(x^{mp}) = \lim_{\epsilon\to 0}\Bigg( & E\sum_{\mathrm{B}^-}\Big(\mathrm{u}_{\mathrm{B}^-}\mathrm{N}'_{\mathrm{B}^-}(x^{mp})\int_{-\epsilon+x_{\mathrm{A}}}^{x_{\mathrm{A}}+\epsilon}\mathrm{N}''_{\mathrm{A}}(x^{mp})(x-x^{mp})\,\mathrm{d}x\Big) + E\sum_{\mathrm{B}^+}\Big(\mathrm{u}_{\mathrm{B}^+}\mathrm{N}'_{\mathrm{B}^+}(x^{mp})\int_{-\epsilon+x_{\mathrm{A}}}^{x_{\mathrm{A}}+\epsilon}\mathrm{N}''_{\mathrm{A}}(x^{mp})(x-x^{mp})\,\mathrm{d}x\Big) \\ & + E\,\mathrm{u}_{\mathrm{A}}\Big(\mathrm{N}'_{\mathrm{A}^-}(x^{mp})\int_{-\epsilon+x_{\mathrm{A}}}^{x_{\mathrm{A}}+\epsilon}\mathrm{N}''_{\mathrm{A}}(x^{mp})(x-x^{mp})\,\mathrm{d}x + \mathrm{N}'_{\mathrm{A}^+}(x^{mp})\int_{-\epsilon+x_{\mathrm{A}}}^{x_{\mathrm{A}}+\epsilon}\mathrm{N}''_{\mathrm{A}}(x^{mp})(x-x^{mp})\,\mathrm{d}x\Big)\Bigg). \end{aligned} \tag{23}$$

Invoking the property of the Dirac distribution the above integrals simplify as follows

$$\begin{aligned}\mathrm{R}_{\mathrm{A}}^{(1)}(x^{mp}) = -\frac{2}{h}\Bigg( & \left(x_{\mathrm{A}}-x^{mp}\right)E\sum_{\mathrm{B}^-}\left(\mathrm{N}'_{\mathrm{B}^-}(x^{mp})\,\mathrm{u}_{\mathrm{B}^-}\right) + \left(x_{\mathrm{A}}-x^{mp}\right)E\sum_{\mathrm{B}^+}\left(\mathrm{N}'_{\mathrm{B}^+}(x^{mp})\,\mathrm{u}_{\mathrm{B}^+}\right) \\ & + \left(x_{\mathrm{A}}-x^{mp}\right)E\,\mathrm{N}'_{\mathrm{A}^-}(x^{mp})\,\mathrm{u}_{\mathrm{A}} + \left(x_{\mathrm{A}}-x^{mp}\right)E\,\mathrm{N}'_{\mathrm{A}^+}(x^{mp})\,\mathrm{u}_{\mathrm{A}}\Bigg). \end{aligned} \tag{24}$$

The factor $2/h$ corresponds to the jump in the gradient of the shape functions at the A−th node oriented along the normal $n^+$, i.e. $\frac{2}{h} = \left(\mathrm{N}'_{\mathrm{A}^+} - \mathrm{N}'_{\mathrm{A}^-}\right)n^+ := [\![\mathrm{N}'_{\mathrm{A}}]\!]\,n^+$. Additionally, the following sums give the elemental values of the stresses

$$E\sum_{\mathrm{B}^-}\left(\mathrm{N}'_{\mathrm{B}^-}(x^{mp})\,\mathrm{u}_{\mathrm{B}^-}\right) = -\sigma^-\,n^+; \tag{25}$$

$$E\sum_{\mathrm{B}^+}\left(\mathrm{N}'_{\mathrm{B}^+}(x^{mp})\,\mathrm{u}_{\mathrm{B}^+}\right) = \sigma^+\,n^+, \tag{26}$$

where different signs on the elemental stresses are due to the different outer normals of the elements. Additionally, the sum of the gradients of the shape functions at the A−th node on different sides gives null contribution, which leads the third and fourth components on the RHS of Eq. (24) to cancel out as follows

$$\left(x_{\mathrm{A}}-x^{mp}\right)E\,\mathrm{N}'_{\mathrm{A}^-}(x^{mp})\,\mathrm{u}_{\mathrm{A}} + \left(x_{\mathrm{A}}-x^{mp}\right)E\,\mathrm{N}'_{\mathrm{A}^+}(x^{mp})\,\mathrm{u}_{\mathrm{A}} = \left(x_{\mathrm{A}}-x^{mp}\right)E\left(\mathrm{N}'_{\mathrm{A}^-}(x^{mp}) + \mathrm{N}'_{\mathrm{A}^+}(x^{mp})\right)\mathrm{u}_{\mathrm{A}} = 0. \tag{27}$$

Eq. (24) then simplifies into

$$\mathrm{R}_{\mathrm{A}}^{(1)}(x^{mp}) = E\sum_{\mathrm{B}}\mathrm{u}_{\mathrm{B}}\int_{x^{mp}-l^{mp}/2}^{x^{mp}+l^{mp}/2}\left(\mathrm{N}'_{\mathrm{A}}(x)\,\mathrm{N}'_{\mathrm{B}}(x)\right)'\Big|_{x^{mp}}(x-x^{mp})\,\mathrm{d}x = -\left(x_{\mathrm{A}}-x^{mp}\right)[\![\mathrm{N}'_{\mathrm{A}}]\!]\,n^+\left([\![\sigma]\!]\,n^+\right), \tag{28}$$

In light of the above equation and of Eq. (18), the internal force computed with the FEM with linear shape functions over the bubble of diameter $l^{mp}$ gives the sMPM internal force vector contribution minus spurious contributions activated by the cell-crossing and high-order terms. In this sense, the goal of the SC-MPM is to cancel out these spurious contributions arising when a MP cross a cell. The term $\mathrm{R}_{\mathrm{A}}^{(1)}(x^{mp})$ does not go to zero with grid refinement (it actually tends to infinity since $[\![\mathrm{N}'_{\mathrm{A}}]\!] = \frac{2}{h}$) nor by increasing the number of MPs per cell, and is the prime cause of cell-crossing instability. As a matter of fact, strategies meant to alleviate this instability are designed to smooth the jump in the shape function second derivatives to avoid a Dirac distribution at the element interfaces (see, for instance, [7–9,53–56]). However, all these alternatives come at the cost of increasing the shape functions' stencil, which has drawbacks as described earlier in the paper. This manuscript pursues a different approach to mitigate the cell crossing instability, which counteracts the oscillating effect given by term $\mathrm{R}_{\mathrm{A}}^{(1)}(x^{mp})$.

As for the residual terms $\mathrm{R}_{\mathrm{A}}^{(q)}(x^{mp})$, it can be demonstrated how these give rise to a convergent (but not absolutely convergence) series. This can be appreciated if expanding further the orders of the Taylor expansions, i.e.,

$$\sum_{q=2}^{\infty}\mathrm{R}_{\mathrm{A}}^{(q)}(x^{mp}) = \underbrace{E\sum_{\mathrm{B}}\left(\mathrm{u}_{\mathrm{B}}\int_{x^{mp}-l^{mp}/2}^{x^{mp}+l^{mp}/2}\left(\mathrm{N}'_{\mathrm{A}}(x)\,\mathrm{N}'_{\mathrm{B}}(x)\right)''\Big|_{x^{mp}}\frac{(x-x^{mp})^2}{2}\,\mathrm{d}x\right)}_{:=\mathrm{R}_{\mathrm{A}}^{(2)}(x^{mp})} + \sum_{q=3}^{\infty}\mathrm{R}_{\mathrm{A}}^{(q)}(x^{mp}). \tag{29}$$

Applying the calculus fundamental theorem, the term $\mathrm{R}_{\mathrm{A}}^{(2)}(x^{mp})$ becomes

$$\begin{aligned}\mathrm{R}_{\mathrm{A}}^{(2)}(x^{mp}) = & -E\sum_{\mathrm{B}}\left(\mathrm{u}_{\mathrm{B}}\int_{x^{mp}-l^{mp}/2}^{x^{mp}+l^{mp}/2}\left(\mathrm{N}'_{\mathrm{A}}(x)\,\mathrm{N}'_{\mathrm{B}}(x)\right)'\Big|_{x^{mp}}(x-x^{mp})\,\mathrm{d}x\right) \\ & + \left[E\sum_{\mathrm{B}}\left(\mathrm{u}_{\mathrm{B}}\left(\mathrm{N}'_{\mathrm{A}}(x)\,\mathrm{N}'_{\mathrm{B}}(x)\right)'\Big|_{x^{mp}}\frac{(x-x^{mp})^2}{2}\,\mathrm{d}x\right)\right]_{x^{mp}-l^{mp}/2}^{x^{mp}+l^{mp}/2}. \end{aligned} \tag{30}$$

Since the boundary term vanishes (the second derivative of the shape functions gives contribution only in correspondence of the A−th node, see Eq. (21) and Fig. 3(c)), the above residual simplifies as follows

$$\mathrm{R}_{\mathrm{A}}^{(2)}(x^{mp}) = -E\sum_{\mathrm{B}}\left(\mathrm{u}_{\mathrm{B}}\int_{x^{mp}-l^{mp}/2}^{x^{mp}+l^{mp}/2}\left(\mathrm{N}'_{\mathrm{A}}(x)\,\mathrm{N}'_{\mathrm{B}}(x)\right)'\Big|_{x^{mp}}(x-x^{mp})\,\mathrm{d}x\right) = -\mathrm{R}_{\mathrm{A}}^{(1)}(x^{mp}), \tag{31}$$

which leads to

$$\sum_{q=1}^{\infty} \mathrm{R}_{\mathsf{A}}^{(q)}\left(x^{mp}\right) = \mathrm{R}_{\mathsf{A}}^{(1)}\left(x^{mp}\right) + \mathrm{R}_{\mathsf{A}}^{(2)}\left(x^{mp}\right) + \sum_{q=3}^{\infty} \mathrm{R}_{\mathsf{A}}^{(q)}\left(x^{mp}\right) = \sum_{q=3}^{\infty} \mathrm{R}_{\mathsf{A}}^{(q)}\left(x^{mp}\right). \tag{32}$$

Since a similar rationale can be applied to $\mathrm{R}_{\mathsf{A}}^{(3)}\left(x^{mp}\right)$ and the other high-order terms to infinity, it can be seen that

$$\left.\mathrm{f}_{\mathsf{A}}^{int,FEM}\right|_{\mathcal{B}}\left(x^{mp}\right) = \sum_{q=0}^{\infty} \mathrm{R}_{\mathsf{A}}^{(q)}\left(x^{mp}\right) = \begin{cases} \mathrm{f}_{\mathsf{A}}^{int,sMPM}\left(x^{mp}\right) & \text{if } \max q \text{ is an even number;} \\ \mathrm{f}_{\mathsf{A}}^{int,sMPM}\left(x^{mp}\right) + \mathrm{R}_{\mathsf{A}}^{(1)}\left(x^{mp}\right) & \text{if } \max q \text{ is an odd number,} \end{cases} \tag{33}$$

with the worst-case scenario in terms of spurious components given by $\max q$ being an odd number.

### *4.2. Regularity issues in the sMPM*

Let us now consider the contribution of a single MP to the internal force vector in the most general $n^{dim}$–dimensional scenario with material and geometrical non-linearities. This contribution can be seen as the result of an integral over the volume of this functions multiplied by the Dirac $\delta_{\boldsymbol{x}^{mp}}$ distribution centred at the MP location, i.e.,

$$v^{mp}\left(\boldsymbol{u}^{mp}\right) \mathbf{grad}\, \delta\Delta^{h}\boldsymbol{u}\left(\boldsymbol{x}^{mp}\right) : \boldsymbol{\sigma}\left(\boldsymbol{\alpha}_{n}^{mp}, \boldsymbol{u}^{mp}\right) = v^{mp}\left(\boldsymbol{u}^{mp}\right) \int_{{}^{h}\hat{\omega}} \delta_{\boldsymbol{x}^{mp}} \underbrace{\mathbf{grad}\left(\delta\Delta^{h}\boldsymbol{u}\left({}^{h}\boldsymbol{x}\right)\right)}_{\in\left(H^{0}\left({}^{h}\hat{\omega}\right)\right)^{n^{dim}\times n^{dim}}} : \underbrace{\boldsymbol{\sigma}\left(\boldsymbol{\alpha}_{n}, {}^{h}\boldsymbol{u}\right)}_{\in\left(H^{0}\left({}^{h}\hat{\omega}\right)\right)^{n^{dim}\times n^{dim}}} \mathrm{d}v, \tag{34}$$

where it is highlighted that the components of the test functions' gradient and the stress (related to the gradient of the trial functions) are in $H^{0}\left({}^{h}\hat{\omega}\right)$. Upon closer examination, the only way for the above equation to hold is if $\delta_{\boldsymbol{x}^{mp}} \in H^{0}\left({}^{h}\hat{\omega}\right)$, which violates the definition of the Dirac distribution (compare with Eq. (21)); these components (of trial and test functions) do not provide sufficient regularity to define a dual space with a negative exponent for the distribution, resulting in an highly-irregular contribution when a MP crosses between elements.

As highlighted in Section 4.1, one way to proceed is to increase the order of the trial and test functions, so that the components of their weak gradients belong at least to $H^{1}\left({}^{h}\hat{\omega}\right)$. This choice enables the components of trial and test function on the RHS of Eq. (34) to be sufficiently regular to define a dual space with negative exponent for the $\delta_{\boldsymbol{x}^{mp}}$ distribution. For these smoother functions, the contribution of each MP is sufficiently regular to mitigate the cell-crossing issue. Conversely, in the SC-MPM presented below, a penalty term (similar to the unstable component $\mathrm{R}_{\mathsf{A}}^{(1)}\left(x^{mp}\right)$ quantified in Eq. (28)) is added to the stationarity of the functional (14) which acts as a weak regularisation on the solution field and of its gradient.

## 5. SC-MPM

In this section the SC-MPM is described. Firstly, the penalty term added to create the SC-MPM is shown to share some similarities with other penalty methods available in the literature, allowing some useful comparisons. Next, since the SC-MPM requires the reconstruction of the stress field on the element facets, mapping techniques are introduced with the goal of reconstructing the stress at these positions. Finally, the few steps required to integrate the SC-MPM into an implicit MPM framework are briefly outlined.

### *5.1. Penalty stabilisation*

Stemming from the sMPM weak form (i.e., Eq. (13)), with the addition of a penalty term at the internal facets of active elements, the new SC-MPM weak form is as follows: given $\boldsymbol{\alpha}_{n}^{mp}$ and $\boldsymbol{u}_{n}^{mp}$, find $\Delta^{h}\boldsymbol{u} \in {}^{h}\mathscr{V}_{\boldsymbol{u}_{D}}\left({}^{h}\hat{\omega}\right)$ s.t.

$$\begin{aligned} &\sum_{K} \sum_{mp|K} \left( v^{mp}\left(\boldsymbol{u}^{mp}\right) \mathbf{grad}\, \delta\Delta^{h}\boldsymbol{u}\left(\boldsymbol{x}^{mp}\right) : \boldsymbol{\sigma}\left(\boldsymbol{\alpha}_{n}^{mp}, \boldsymbol{u}^{mp}\right) - m^{mp}\, \delta\Delta^{h}\boldsymbol{u}\left(\boldsymbol{x}^{mp}\right) \cdot \boldsymbol{b}\left(\boldsymbol{x}^{mp}\right) \right) \\ &+\beta \sum_{F\in\mathcal{F}^{in}\left({}^{h}\mathcal{T}^{act}\right)} \int_{\gamma_{F}} [\![\mathbf{grad}\, \delta\Delta^{h}\boldsymbol{u}]\!] \cdot \boldsymbol{n}^{+} \cdot [\![\boldsymbol{\sigma}]\!] \cdot \boldsymbol{n}^{+}\, \mathrm{d}a = 0, \quad \forall \delta\Delta^{h}\boldsymbol{u} \in {}^{h}\mathscr{V}_{\boldsymbol{0}}\left({}^{h}\hat{\omega}\right), \end{aligned} \tag{35}$$

where $\beta > 0$ is a user-selected penalty factor and the jump operator across the facets implies $[\![(\bullet)]\!] = (\bullet)^{+} - (\bullet)^{-}$. The normal to the facet in the outer direction with respect to the positive element is denoted with $\boldsymbol{n}^{+}$. The additional penalty term is integrated with standard Gauss–Legendre quadrature at all facets $F \in \mathcal{F}^{in}\left({}^{h}\mathcal{T}^{act}\right)$ (see Fig. 2(b)).

Removing the dependency from the test functions' coefficients and expressing the trial discrete functions in ${}^{h}\mathscr{V}_{\boldsymbol{u}_{D}}\left({}^{h}\hat{\omega}\right)$ as $\Delta^{h}\boldsymbol{u}\left(\boldsymbol{x}^{mp}\right) = \sum_{\mathsf{A}} \mathrm{N}_{\mathsf{A}}\left(\boldsymbol{x}^{mp}\right) \Delta\mathbf{u}_{\mathsf{A}}$, the discrete weak form of the SC-MPM is given by: given $\boldsymbol{\alpha}_{n}^{mp}$ and $\boldsymbol{u}_{n}^{mp}$, find $\Delta\mathbf{u}_{\mathsf{A}}$ s.t.

$$\begin{aligned} &\overbrace{\sum_{K} \sum_{mp|K} \left( v^{mp}\left(\boldsymbol{u}^{mp}\right) \mathbf{grad}\left(\mathrm{N}_{\mathsf{A}}\left(\boldsymbol{x}^{mp}\right)\mathbf{1}\right) : \boldsymbol{\sigma}\left(\boldsymbol{\alpha}_{n}^{mp}, \boldsymbol{u}^{mp}\right) \right)}^{:=\mathbf{f}_{\mathsf{A}}^{int,sMPM}} - \overbrace{\sum_{K} \sum_{mp|K} \left( m^{mp}\, \mathrm{N}_{\mathsf{A}}\left(\boldsymbol{x}^{mp}\right) \cdot \boldsymbol{b}\left(\boldsymbol{x}^{mp}\right) \right)}^{:=\mathbf{f}_{\mathsf{A}}^{ext,sMPM}} \\ &\underbrace{+\beta \sum_{F\in\mathcal{F}^{in}\left({}^{h}\mathcal{T}^{act}\right)} \sum_{gp|F} a_{F}\, [\![\mathbf{grad}\, \mathrm{N}_{\mathsf{A}}\left(x^{gp}\right)\mathbf{1}]\!] \cdot \boldsymbol{n}^{+} \cdot [\![\boldsymbol{\sigma}\left(x^{gp}\right)]\!] \cdot \boldsymbol{n}^{+}}_{:=\mathbf{f}_{\mathsf{A}}^{pen}} = 0, \end{aligned} \tag{36}$$

where $gp|F$ are the facets' Gauss Points (GPs) at the $x^{gp}$ position and $a_F$ is the facets' area.

It can be seen how this additional penalty term $\mathbf{f}_{\mathsf{A}}^{pen}$ is similar to the spurious contribution $\mathrm{R}_{\mathsf{A}}^{(1)}(x^{mp})$ (see Eq. (28)) due to the cell-crossing issue, but with different sign to counteract it.

The above penalty term shares similarities with the face ghost penalty method (see Burman [15] for the original work, Sticko et al. [57] for an application to unfitted FEM solid mechanics and Coombs [12] for its application to the MPM) and one of the penalties (specifically, $\mathscr{J}_1$ in Eq. (11)) suggested by Liu et al. [58] for unfitted interface elliptic problems. However, the penalty term in Eq. (35) differs from the above-listed terms in the literature in three key aspects: (i) the jump in the gradient of trial functions is substituted by the jump in the stresses; (ii) the integral is applied to *all* the internal facets; and (iii) the above term does not scale *only* with the grid size.

The modification proposed in (i) is significant not only for geometrically non-linear problems, where the relationship between stress and strain is more complex than standard infinitesimal linear elasticity, but also for cases involving material non-linearity, such as plasticity. Therefore, this modification is applicable to a wide range of scenarios that involve different materials within the framework of finite strain mechanics.

The ghost penalty method states that a penalty term must be added to the facets between active elements on the boundary of the material and to their neighbouring active elements (compare with [12]). However, the penalty term of the SC-MPM is applied to all the internal facets (point (ii)), thus including those envisaged by the ghost penalty method (see, again, Fig. 2(a)). This choice is motivated by the aim of mitigating the cell-crossing instability, which can occur anywhere in the active grid domain. However, this choice has other consequences. On one hand, it automatically removes the small-cut issue that the ghost penalty method resolves, thereby inheriting this stability into the SC-MPM. On the other hand, it makes the method more sensitive to the choice of the parameter $\beta$. If strongly enforced (i.e., $\beta \to +\infty$), the above term is known to force the solution to lie on a plane, resulting in locking (see Badia et al. [59] for an explanation of the phenomenon in the case of unfitted FEM). This is not a desirable feature, which makes careful tuning of $\beta$ more critical than in the standard ghost penalty approach

The penalty term in Eq. (35) is expected to scale proportionally with a length measure according to physical units. In this sense, Eq. (28) can be used as a proxy for quantifying the parameter $\beta$. The residual $\mathrm{R}_{\mathsf{A}}^{(1)}(x^{mp})$ is a spurious contribution seen every time a MP cross a cell. However, because of the way the MPM finds incremental solutions and uses them to compute a total value of the deformation gradient, this spurious contribution, initially proportional to the distance between the MP and the node, propagates and increases throughout the time of the simulation. Owing to this incrementally propagating spurious contribution, the following inequalities hold

$$|x_{\mathsf{A}} - x^{mp}| = |x_{\mathsf{A}} - X^{mp} - u^{mp}| \leq |x_{\mathsf{A}} - X^{mp}| + |u^{mp}| \leq |h| + |u^{mp}|. \tag{37}$$

Since a single parameter valid globally throughout the grid is desired for simplicity, then

$$|h| + |u^{mp}| \leq |h| + \max_{mp} |u^{mp}|. \tag{38}$$

To avoid a dependency on the current displacement $u^{mp}$ that would create additional terms in the linearisation required for the iterative process, the maximum value of the current displacement can be relaxed to the previously-converged one $u_n^{mp}$, which justifies (in multiple dimensions) the current $\beta$ to be

$$\beta = \|\boldsymbol{h}\| + \max_{mp} \|\boldsymbol{u}_n^{mp}\|. \tag{39}$$

Numerical experiments (see Sections 6.1 and 6.2) that compare $\beta$ from Eq. (39) with values of $\beta$ fixed during the entire simulations support the above rationale. It must also be noted that Eq. (39) considers both the selected discretisation (via the grid size $\boldsymbol{h}$) and the specific problem under consideration (via the previously-converged maximum absolute value of the MP's displacement $\boldsymbol{u}_n^{mp}$).

### *5.2. Reconstruction of the historical variables*

In the MPM, the only points which store historical variables for the problem domain are the MPs. However, the additional penalty term requires the stress field at the location of the GPs, which lie on the facets belonging $F \in \mathcal{F}^{in}({}^{h}\mathcal{T}^{act})$ (see Eq. (35) and Fig. 2(b)). Hence, mappings are required to reconstruct the stress field at these positions where the stress variables are not stored. Additionally, since the facets of the grid elements can become active and inactive during a simulation, initialising and storing historical variables at the GPs would provide uncorrected stress values because these GPs might have undergone a different loading process to the MPs.

Any mapping procedure requires some weights to mediate the values coming from the initial source of points (the MPs, in this case). This method adopts weights that are the product of the shape function (to account for the distance of the source point from the nodes' facet) and the MPs' volume (to account for each MP being representative of a portion of volume),[8] i.e.,

$$\mathrm{w}_{\mathsf{A}}^{mp} = \frac{\mathrm{N}_{\mathsf{A}}\left(\boldsymbol{x}^{mp}\right) v^{mp}}{\left(\sum_{mp|K} \mathrm{N}_{\mathsf{A}}\left(\boldsymbol{x}^{mp}\right) v^{mp}\right)}. \tag{40}$$

---

[8] The choice of mapping (40)–(43), while not unique, strikes a balance between accuracy, simplicity, and computational efficiency. Exploration of alternative mapping processes, such as that proposed by Mota et al. [60] (see also the references therein), or Moving Least Squares (see, e.g., Sulsky and Gong [9]) is not considered here. Despite this consideration on the considered mappings, it is essential to note that mappings (40)–(43) serve to inform the penalty term in the SC-MPM. While this term impacts the solution at the grid nodes and the stress at the MPs, it lacks any physical significance. Therefore, the mappings needed for its initial reconstruction are not bound by any conservation properties. This is in contrast, for instance, with the mapping of initial velocity field in the case of dynamic formulations (see Love and Sulsky [61] and in Pretti et al. [48]).

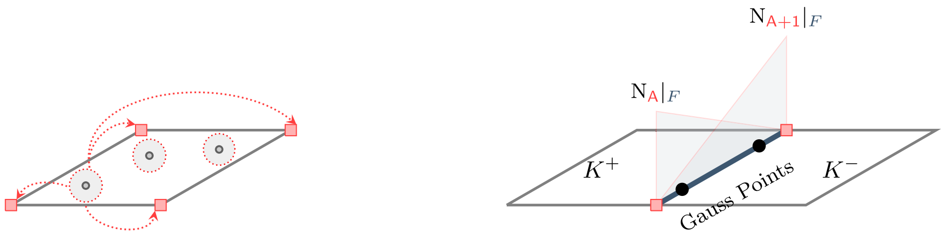

(a) The variables required to reconstruct the penalty term (A.1) are moved via Eqs. (40)-(43) from the MPs in an element to the grid nodes.

(b) For a given face, the same variables are then moved from the nodes to the GP locations via the shape functions restricted to the selected face.

**Fig. 4.** The two step procedure to map the variables required to construct the penalty term in Eq. (A.1).

To make the stress field a function of the current displacement for the hyperelastic material described by Eqs. (3)–(6), it is more convenient to reconstruct not so much the stresses directly, but the other quantities on which the stresses depend. This choice is also motivated by assuming a unique constitutive relationship between MPs and GPs. The above weights are thus used to reconstruct the historical variables required to compute a stress field for the considered material, these being the previously converged elastic logarithmic strain, the previously-converged deformation gradient, and any set of internal variables considered in Eq. (3), (see Simo [46,47] for algorithmic details) i.e.,

$$\left(\boldsymbol{\epsilon}^e_n\right)_{\mathsf{A}} = \sum_{mp|K} \mathrm{w}^{mp}_{\mathsf{A}} \left(\boldsymbol{\epsilon}^e_n\right)^{mp}; \tag{41}$$

$$\left(\boldsymbol{F}_n\right)_{\mathsf{A}} = \sum_{mp|K} \mathrm{w}^{mp}_{\mathsf{A}} \boldsymbol{F}^{mp}_n; \tag{42}$$

$$\left(\boldsymbol{\alpha}_n\right)_{\mathsf{A}} = \sum_{mp|K} \mathrm{w}^{mp}_{\mathsf{A}} \boldsymbol{\alpha}^{mp}_n. \tag{43}$$

Having employed weights depending on the shape functions, the reconstructed variables are centred at the grid nodes (see Fig. 4(a)), and each of their components is $C^0({}^h\hat{\omega})$ due to the continuity guaranteed by the linear shape functions (see Eq. (12)). The use of the facet's shape functions (Fig. 4(b)) permits movement of these variables at the locations of the GPs on the facets, where the initialisation of the penalty term of the SC-MPM is completed by calling the constitutive relationship. Because of the above-mentioned continuity of the shape functions, each component of the stress at the 0−th iteration of the Newton–Raphson (NR) is equal on each side of the neighbouring elements sharing a given facet, making the stress jump zero. This choice minimises the impact of the penalty term in the SC-MPM. As the incremental solution develops with the subsequent NR iterations, jumps in the incremental gradients will appear and so the penalty will start to be non-zero and affect the solution. This gradual role of the penalty in the SC-MPM provides its effectiveness in regularising the stress field without spoiling the solution. However, this regularisation can be undesirable when localised features, such as shear bands, are intended to form. Both of these points (i.e., smooth stress field and shear bands) are investigated by the numerical examples presented in Section 6.

### *5.3. Implementation details*

This section briefly details the additional computations (and their position among the phases of the MPM algorithm) required by the SC-MPM. The additional operations are:

- Phase (i): for each time-step, initialise the GPs' quantities for each facet $F \in \mathcal{F}^{in}\left({}^h\mathcal{T}^{act}\right)$;
- Phase (ii): for each time-step, reconstruct the variables necessary for stress employing Eqs. (40)–(43);
- Phase (iii): for each NR iteration, assemble the additional penalty terms (using the nodal updated incremental displacement) and its contribution to Jacobian matrix of the NR process (Appendix A provides its linearisation).

To better contextualise the above steps in an MPM algorithm, the reader can refer to Algorithm 1. These changes have been implemented in the open-source MPM code AMPLE (A Material Point Learning Environment) [50] and this is used in the numerical examples that follow.

## 6. Numerical examples

This section presents three numerical examples that involve both elastic and elasto-plastic materials, tested over a range of different grid sizes and elements. Comparisons are made with the sMPM and the GIMPM. In the case of quad elements, MPs are initially evenly distributed in each direction. For simplex elements, MPs are initialised similarly to those of quad elements and Duffy's rule [62] is then applied to map the points (and relative volumes) originally belonging to a quad element to the respective

**Algorithm 1:** SC-MPM pseudo-code. Additional steps required only for the SC-MPM are highlighted by the grey-coloured background. MPs (or GPs) indicates the loop over MPs (or GPs). When these loops call the constitutive relationship, a background dashed pattern is added (e.g., MPs).

```
⇒ Preprocessing;
Set step counter $n+1=0$;
while $n+1 <= N^{stps}$ (loop over simulation steps) do
    Identify active grid elements, $K \in {}^{h}\mathcal{T}^{act}$;
    P2G mapping (including variables via Eqs. (40)-(43)) MPs ;
    Identify internal facets $F \in \mathcal{F}^{in}\left({}^{h}\mathcal{T}^{act}\right)$;
    Initialise GPs GPs ;
    Assemble $\mathbf{f}_{\mathsf{A}}^{ext,sMPM}$, Eq. (36) MPs ;
    Set NR counter $k_{n+1}=0$;
    while $criterion > tol$ (NR iterative loop) do
        if $k_{n+1}>0$ then
            Compute incremental solution $\Delta^{h}\boldsymbol{u}$;
        end
        Assemble $\mathbf{f}_{\mathsf{A}}^{int,sMPM}$ Eq. (36), and contribution to tangent matrix MPs ;
        Assemble $\mathbf{f}^{pen}$ Eq. (36), and contribution to tangent matrix Eqs. (A.15)-(A.18) GPs ;
        Compute NR residual $\mathbf{r}_{\mathsf{A}}=\mathbf{f}_{\mathsf{A}}^{int,sMPM}-\mathbf{f}_{\mathsf{A}}^{ext,sMPM}+\mathbf{f}^{pen}$ and $criterion$;
        Update NR counter $k_{n+1}$;
    end
    G2P mapping MPs ;
    Postprocessing ⇐;
    Update step counter $n+1$;
end
```

points (and volumes) in a triangle (see, for more details, [63]). To avoid issues related to small cuts, the penalty term from the SC-MPM is used as a ghost penalty method for both the sMPM and the GIMPM, applying it only at the interfaces between active boundary elements and their neighbouring active elements. Since the SC-MPM uses linear shape functions, two GPs ($gp|F=2$) are employed at the interfaces for the quadrature rule.

To compare the results, two different types of error measure are employed: local measures defined at MPs, i.e.,

$$e^{mp,(\bullet)} := \frac{\| (\bullet)_{num}^{mp} - (\bullet)_{analyt}^{mp} \|}{\| (\bullet)_{analyt}^{mp} \|}, \tag{44}$$

and global measures, i.e.,

$$e^{(\bullet)} := \frac{\sum_{mp} \| (\bullet)_{num}^{mp} - (\bullet)_{analyt}^{mp} \| \, {}^{0}v^{mp}}{\sum_{mp} \| (\bullet)_{analyt}^{mp} \| \, {}^{0}v^{mp}}. \tag{45}$$

In the above equations, $(\bullet)_{num}^{mp}$ denotes the quantity $(\bullet)$ coming from numerical analyses and sampled at the MPs' position and $(\bullet)_{analyt}^{mp}$ the numerical value sampled in the same position. ${}^{0}v^{mp}$ is the MP's initial volume.

All the numerical examples are solved using a NR iterative process, where the additional terms in the linearised system due to the penalty term $\mathbf{f}^{pen}$ (see Appendix A) are added to those of the standard internal force vector. According to Algorithm 1, the residual $\mathbf{r}$ is computed at each NR iteration. Specifically, this manuscript, similarly to Coombs and Augarde [50], chooses to compute the criterion of the NR as follows

$$criterion = \frac{\|\mathbf{r}\|}{\|\mathbf{f}^{ext,sMPM}+\mathbf{f}^{rct}\|}, \tag{46}$$

where $\mathbf{f}^{rct}$ are the reaction forces due to the strong imposition of Dirichlet BCs. This criterion value is checked against a tolerance set to $tol = 1\times10^{-6}$.

### *6.1. Mono-dimensional column under self-weight*

*Example scope.* The scope of the example represented in Fig. 5 is fourfold: (i) to investigate the role of the parameter $\beta$ for the SC-MPM formulation; (ii) to compare the SC-MPM with sMPM and GIMPM against an analytical stress solution, in the context of

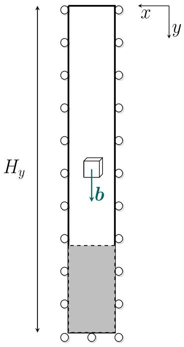

**Fig. 5.** Graphical illustration of the mono-dimensional column under self-weight. The figure also reports the qualitative ratio between the initial (white) and final (grey) configurations.

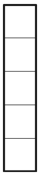

**Fig. 6.** Initial discretisation for quad elements in the case of $n^{els,y} = 5$.

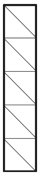

**Fig. 7.** Initial discretisation for simplex elements in the case of $n^{els,y} = 5$.

finite elastic and elasto-plastic mechanics; (iii) to examine the stress-convergence of the methods with grid refinement; and (iv) compare the runtime of the SC-MPM with those of sMPM and GIMPM. To study (i), a set of elastic analyses (labelled set ($a$)) with $\beta$ spanning 1.5 orders of magnitude has been run and compared against the adaptive formula Eq. (39). A second set of elastic and elasto-plastic simulations, denoted as set ($b$), has been setup to explore the scopes (ii)-(iv). For (ii) the analytical solution outlined in Charlton et al. [51] is used for both the elastic and the elasto-plastic cases. Grids spanning 3 order of magnitudes for linear quad and simplex (linear triangular) elements have been employed to investigate (iii) and (iv).

*Setup.* Set ($a$) of analyses have been run considering an elastic Hencky material $E = 1 \times 10^4$ Pa and $\nu = 0$, making the simulations entirely mono-dimensional stress-wise. The gravitational acceleration $\boldsymbol{b} = [0, g]^T$ has been linearly increased from 0 to 10 m s$^{-2}$ over 40 pseudo-time steps. The initial density of the material is 300 kg m$^{-3}$, while the initial height $H_y$ is 50 m. Rollers are applied everywhere on the boundary, with the exception of the top boundary, which is homogeneous Neumann. To vertically discretise this setup, the analyses employ 160 quad elements vertically, with initially 2 MPs per element per direction. In set ($a$) the penalty parameter takes either fixed values of $\beta$ belonging to the vector $[1, 5, 10, 50, 100, 500]$ m or the adaptive formula Eq. (39).

Set ($b$) involves elastic and elasto-plastic simulations, varying the number of vertical elements according to the vector $\boldsymbol{n}^{els,y} = [5, 10, 50, 100, 500, 1000, 500]$, where $\dim(\boldsymbol{n}^{els,y}) = N$. The grid discretisations for the case of $n^{els,y} = 5$ are shown in Fig. 6 for quad elements and Fig. 7 for simplex elements. The elastic simulations share the same setup as those of set ($a$). The elasto-plastic analyses share the same material as the elastic set, with the exception that a von Mises yield function governs associated plasticity according to the law

$$\Phi(\boldsymbol{\tau}) = \frac{\sqrt{2\,J_2}}{\rho_y} - 1 = 0, \tag{47}$$

with $J_2 = \frac{1}{2}\boldsymbol{s} : \boldsymbol{s}$, $\boldsymbol{s} = \boldsymbol{\tau} - \frac{1}{3}\boldsymbol{\tau} : \mathbf{1}$, and $\rho_y = 1.25 \times 10^4$ Pa. Owing to non-linear material behaviour, 60 pseudo time-steps are used, over which the gravitational load is linearly increased. All simulations in set ($b$) consider the adaptive formula Eq. (39) for $\beta$. In the case of quad elements, sMPM, SC-MPM and GIMPM are considered. Since the implementation of the GIMPM for simplex elements is

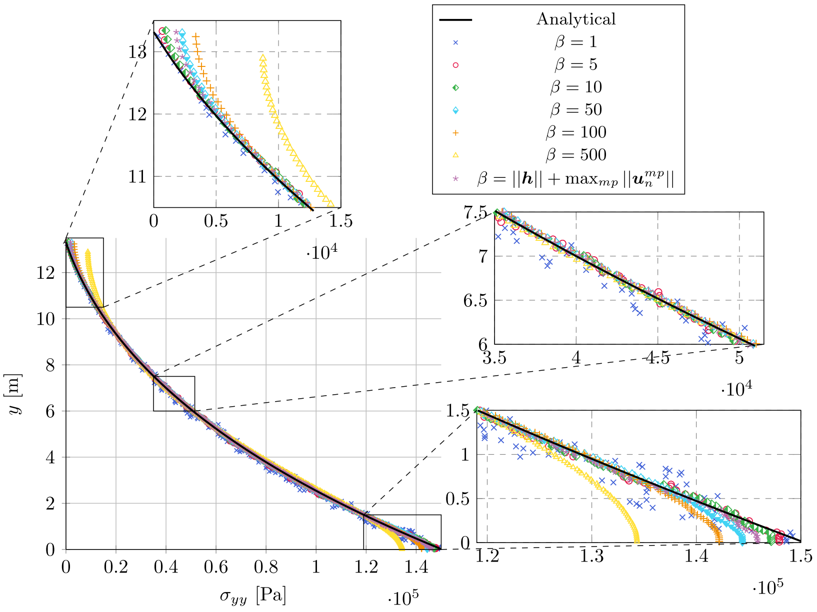

**Fig. 8.** Vertical stress for the mono-dimensional column under self-weight for different values of $\beta$ computed with the SC-MPM with quad elements. The number of vertical elements is $n^{els,y} = 160$.

**Table 1**
Résumé of the error values for the simulations in Fig. 9.

| $\beta$ [m] | $e^{\sigma_{yy}}$ |
|---|---|
| 1 | $\approx 2.09 \times 10^{-2}$ |
| 5 | $\approx 5.74 \times 10^{-3}$ |
| 10 | $\approx 4.11 \times 10^{-3}$ |
| 50 | $\approx 3.98 \times 10^{-3}$ |
| 100 | $\approx 6.72 \times 10^{-3}$ |
| 500 | $\approx 2.68 \times 10^{-2}$ |
| Eq. (39) | $\approx 3.63 \times 10^{-3}$ |

more intricate,[9] only sMPM and SC-MPM are run in this case. The update of the GIMPM characteristic domain follows that proposed by Charlton et al. [51] based on the principal stretches. To compare the runtimes of the simulations, Durham University's Hamilton HPC service has been employed, using MATLAB R2021a running on a Rocky linux 8 operating system on a shared standard node with 32 cores and 128 GB of RAM.

*Results discussion.* Fig. 8 and Table 1 report the results for set ($a$) of simulations. Specifically, Fig. 8 shows the different vertical stress trends depending on the value of $\beta$. From the figure, it is clear that higher values, i.e., $\beta = 100 - 500$ m, tends to produce a smooth solution in the middle of the column. However, these higher penalty values spoil the solution at the top and bottom of the column, as is clear in the magnifications in Fig. 8. An opposite trend is shown by lower values of the penalty (i.e., $\beta = 1 - 10$ m), which do not suppress the oscillation in the middle of the column but tend to produce results closer to the analytical solution at the extremes. The results from the adaptive formula Eq. (39) seem to provide good results, mildly modifying the solution at extreme of the column while giving no oscillation in its middle.

The qualitative behaviours in Fig. 8 are confirmed by the global error values $e^{\sigma_{yy}}$ reported in Table 1 and graphically reproduced in Fig. 9 for the different values of $\beta$. Specifically, Fig. 9 captures that the values $\beta = 10 - 50$ provide a stable region of the error, which tends to increase significantly when moving away from these value. The results of the adaptive formula Eq. (39) fall within this stable region and, for the problem under consideration, provide the lowest value of the global error.

It must be noted that this need to balance between the instabilities suppression and representing the correct values at the boundaries is shared with other stabilisation techniques. This is, for instance, the case of the stabilisation proposed by Brezzi and Pitkäranta [64] (see the discussion in Boffi et al. [65] on this topic). To comply with the inf-sup condition, these authors proposed a stabilisation for pressures in the context of Stokes equations for the conforming FEM. The SC-MPM exhibits this similar

---

[9] To the best of the authors' knowledge, the GIMPM for simplex elements is unavailable in the literature. This lack is likely due to the more challenging implementation for these elements. Conversely, quad elements for structured grids can exploit the alignment between local and global coordinate systems per each Cartesian dimension, decreasing the complexity of the implementation.

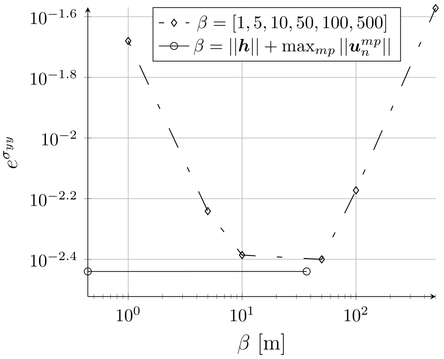

**Fig. 9.** Final global error of vertical stress for different values of $\beta$ (log-log scale): comparison between assigned values of $\beta$ and adaptive formula from Eq. (39).

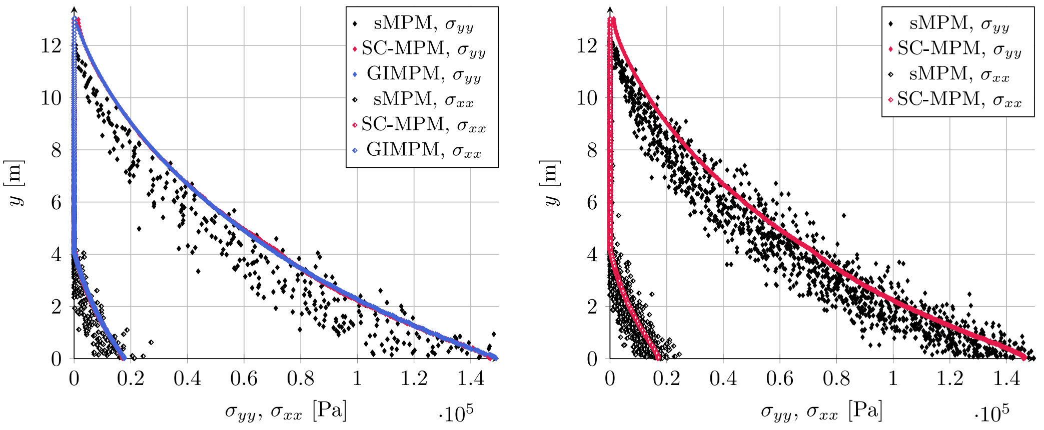

(a) Vertical and horizontal stresses along the depth of the column for quad elements.

(b) Vertical and horizontal stresses along the depth of the column for simplex elements.

**Fig. 10.** Vertical and horizontal stresses for the elasto-plastic mono-dimensional column under self-weight for quad (left) and simplex (right). The number of vertical elements is $n^{els,y} = 160$ and the parameter $\beta$ is adapted according to Eq. (39).

behaviour because the elements at the boundary of the material simultaneously experience two different influences: the imposition of a boundary condition relevant to the specific problem under consideration, and the application of the SC-MPM penalty term on a different facet of the same element. These two conditions are imposed on the same element, which can only accommodate a linear variation of the incremental solution and a constant value of its gradients. This results in an overconstrainment of the element on the boundary of the material. This phenomenon is also linked to the mildly sub-linear convergence rate of the SC-MPM. Specifically, (see Table 2) the simplex elements are constrained to a lesser degree than the quad ones thanks to their setup (compare Fig. 6 with 7). However, a qualitative comparison of the stresses along the depth of the column for the elasto-plastic case (see Figs. 10(a) and 10(b)) demonstrates the dramatic improvement of the SC-MPM over the sMPM, both for quad and simplex elements. In the case of quad elements (see Fig. 10(a)), the difference in stresses between the SC-MPM and the GIMPM at the top and bottom of the column is mildly visible.

While this issue at the extremes of the domain suggests a potential area for improvement, grid convergence analysis on set ($b$) of simulations (see Figs. 11(a) and 11(b)) indicates that the error at the top of the column does not compromise convergence for the SC-MPM. From these figures, the overall trends can be observed, concluding that, for the stress errors,

- sMPM stagnates, despite of grid refinement;
- GIMPM convergences with grid refinement;
- SC-MPM convergences with grid refinement.

To better quantify the above trends, two averaged measures are introduced, these being the averaged slope, denoted $m$, and the local (among three points) Menger curvature, indicated by $\chi$. These quantities are defined as follows

$$m^{(\bullet),(\blacksquare)} := \frac{1}{N}\sum_{i=2}^{N} m^{(\bullet),(\blacksquare)}_{[i,i-1]}, \qquad \text{with} \quad m^{(\bullet),(\blacksquare)}_{[i,i-1]} := \frac{\log e_i^{(\bullet)} - \log e_{i-1}^{(\bullet)}}{\log(\blacksquare)_i - \log(\blacksquare)_{i-1}}; \tag{48}$$

**Table 2**
Summary of the average slopes and maximum absolute curvatures in Figs. 11(a) (quad elements) and 11(b) (simplex elements) for the mono-dimensional consolidation test in the elastic and elasto-plastic cases. Negative values of the curvatures are indicated in red.

| | | Quad elements | | Simplex elements | |
|---|---|---|---|---|---|
| | | Elastic | Plastic | Elastic | Plastic |
| sMPM | $m^{\sigma,n_y^{els}} \approx$ | 0.09 | 0.04 | 0.06 | 0.01 |
| | $\max\left(\lvert\chi^{\sigma,n_y^{els}}\rvert\right) \approx$ | 0.59 | 0.64 | 0.55 | 0.45 |
| SC-MPM | $m^{\sigma,n_y^{els}} \approx$ | −0.88 | −0.78 | −0.95 | −0.75 |
| | $\max\left(\lvert\chi^{\sigma,n_y^{els}}\rvert\right) \approx$ | 0.24 | 0.42 | 0.15 | 0.31 |
| GIMPM | $m^{\sigma,n_y^{els}} \approx$ | −1.21 | −1.08 | – | – |
| | $\max\left(\lvert\chi^{\sigma,n_y^{els}}\rvert\right) \approx$ | 0.14 | 0.3 | – | – |

$$\chi_{[i,i-2]}^{(\bullet),(\blacksquare)} := \frac{4A_{[i,i-2]}}{d\left(P_i^{(\bullet),(\blacksquare)}, P_{i-1}^{(\bullet),(\blacksquare)}\right) d\left(P_i^{(\bullet),(\blacksquare)}, P_{i-2}^{(\bullet),(\blacksquare)}\right) d\left(P_{i-1}^{(\bullet),(\blacksquare)}, P_{i-2}^{(\bullet),(\blacksquare)}\right)}, \qquad \text{with} \quad P_i^{(\bullet),(\blacksquare)} := \left(\log\left(\blacksquare\right)_i, \log(e_i^{\bullet})\right) \tag{49}$$

where $A_{[i,i-2]}$ is the area of the triangle defined by the points $(P_i^{(\bullet),(\blacksquare)}, P_{i-1}^{(\bullet),(\blacksquare)}, P_{i-2}^{(\bullet),(\blacksquare)})$, and $d\left(P_i^{(\bullet),(\blacksquare)}, P_{i-1}^{(\bullet),(\blacksquare)}\right)$ is the Euclidean distance between two of the considered points. The different values of $m^{\sigma,n_y^{els}}$ and the maximum absolute values of $\chi^{\sigma,n_y^{els}}$ resulting from the analyses are reported in Table 2. Based on these data, it can be seen that the sMPM can be slightly diverging (positive slope) or converging (negative slope) depending on the simulation and the selected value of slope. However, despite the single values, the average slope of the sMPM lines only affects the second decimal place beyond zero of these slopes, which is why it can be concluded that sMPM *de facto* stagnates. For this reason, the analysis average curvature $\chi^{\sigma,n_y^{els}}$ provides non-indicative results. Conversely, the GIMPM converges at a superlinear rate.[10] These results are confirmed in the literature for very similar setups (see Charlton et al. [51] and Coombs and Augarde [50]). More specifically, the slopes in the elastic case are initially superlinear, but they flatten progressively towards unity and are overall $-1.21$ for the considered analyses. This is also confirmed by the small value of the maximum absolute curvature, with a value equal to $0.14$. The elasto-plastic case with GIMPM exhibits instead a less steep initial values of slope, resulting in an overall trend close to $m^{\sigma,n_y^{els}} = -1.08$. Lastly, the proposed SC-MPM formulation converges almost linearly in the elastic case (approximately $-0.88$ for quad elements and $-0.95$ for simplex elements), showing a trend which reflects that of a conforming FEM analysis with linear shape functions. This convergence is less steep in the elasto-plastic case (approximately $-0.78$ for quad elements and $-0.75$ for simplex), which, even though as not good as that of the elastic case, confirms that the historical variables reconstruction Eqs. (40)–(43) provide a good estimate for the values at the facets between elements. It must also be noted that the maximum absolute curvatures between the SC-MPM and the GIMPM behave similarly both for the elastic and elasto-plastic case. This indicates that the maximum absolute variation of the slopes of the lines behaves similarly between the two methods. These results are highly significant because, to the best of the authors' knowledge, they demonstrate the first numerical convergence using linear shape functions with a penalty modification of the original MPM (i.e., the SC-MPM[11]). It must also be pointed out that, for triangular elements, the lack of symmetry in the discretisation (compare with Fig. 7 for the case of $n^{els,y} = 5$) introduces spurious shear stresses even in the elastic case, where the analytical solution dictates only the presence of $\sigma_{yy}$. However, Fig. 11(b) confirms that this source of error does not affect the convergence properties, with the error $e^{\sigma}$ constantly being slightly above the error $e^{\sigma_{yy}}$.

Fig. 12(a) displays the runtimes for the simulations across the various grid refinements spanned for simulations $(b)$. It is evident that simulations with simplex elements are slightly more expensive, which is caused by the larger number of cells (compare Figs. 6 and 7 and relative MPs). Interestingly, the most time-consuming simulation arises from the sMPM method using simplex elements in the elasto-plastic case, whereas the cheapest one is provided by the GIMPM using quad elements in the elastic case. These trends are supported by the average NR iterations per step shown in Fig. 12(b), where the sMPM, presenting cell-crossing and oscillatory behaviour, struggles the most to converge. In codes based on implicit MPM solvers, particularly when dealing with a large number of DoFs, the bottleneck is typically the linear solver rather than the loop over MPs (or facets' GPs), which can be easily parallelised. At the same time, the linear solver's performance is influenced by the bandwidth of the tangent matrix. In this mono-dimensional setup, the bandwidth is relatively small. Consequently, even the GIMPM analyses — which involve larger stencils and thus a greater bandwidth — complete their computations in shorter runtimes compared to those requiring additional NR iterations for the sMPM method. Hence, for this specific setup, the increase in NR iterations leads to longer computational times for the problem. Fig. 12(a) also highlights that the SC-MPM scales linearly in a log–log scale of $n_y^{els}$ versus runtime, similarly to the sMPM and the GIMPM. This means that the more costly loop over the facets' GPS (each of which calls the constitutive relationship) does not significantly burden the SC-MPM, keeping its time costs consistent with those of the other methods.

---

[10] The GIMPM is expected to converge at a rate bigger than the SC-MPM because the GIMPM is locally a higher-order method, employing piece-wise linear and second-order shape functions. Conversely, the SC-MPM employs only piece-wise linear shape functions, thus qualifying as a low-order method when compared with GIMPM.

[11] The literature has also proposed the Staggered Grid MPM (SGMPM) [66], to mitigate the cell-crossing instability while maintaining the compact stencils. However, for a mono-dimensional column under self-load similar to that presented in this section, the SGMPM exhibits stagnation with grid refinement. This further remarks on the positive results of the SC-MPM, since avoiding cell-crossing with a compact shape functions' stencil and achieving numerical convergence has been a longstanding challenge in the MPM literature.

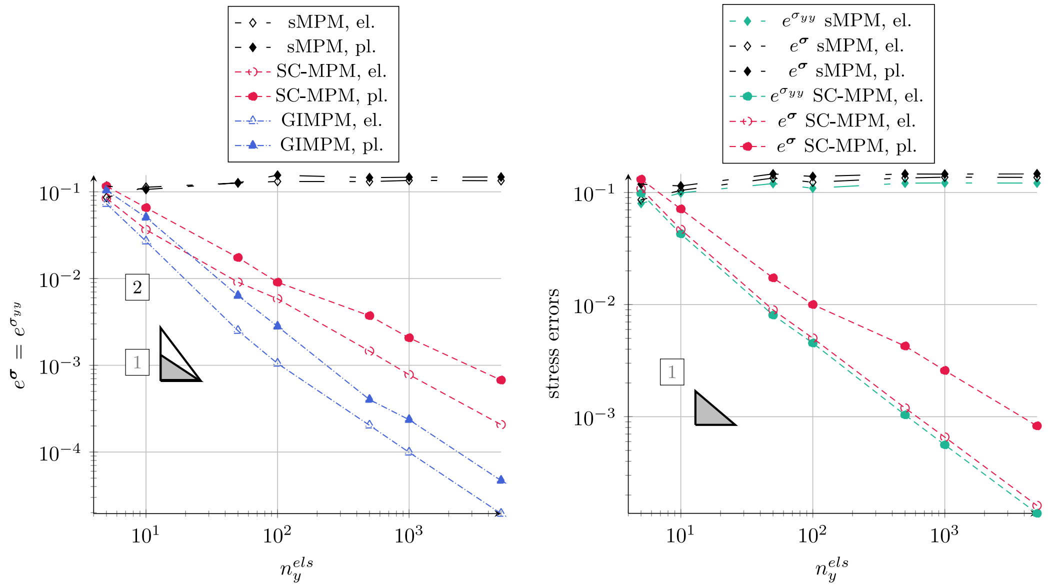

(a) Error convergence (log-log scale) for mono-dimensional column under self-weight for quad elements. The selected value of $\beta$ is 50 m for the sMPM and GIMPM, while the SC-MPM uses the adaptive formula Eq. (39).

(b) Error convergence (log-log scale) for mono-dimensional column under self-weight for simplex elements. The selected value of the $\beta$ is 50 m for the sMPM and GIMPM, while the SC-MPM uses the adaptive formula Eq. (39).

**Fig. 11.** Error convergence comparison for quad (left) and simplex (right) elements.

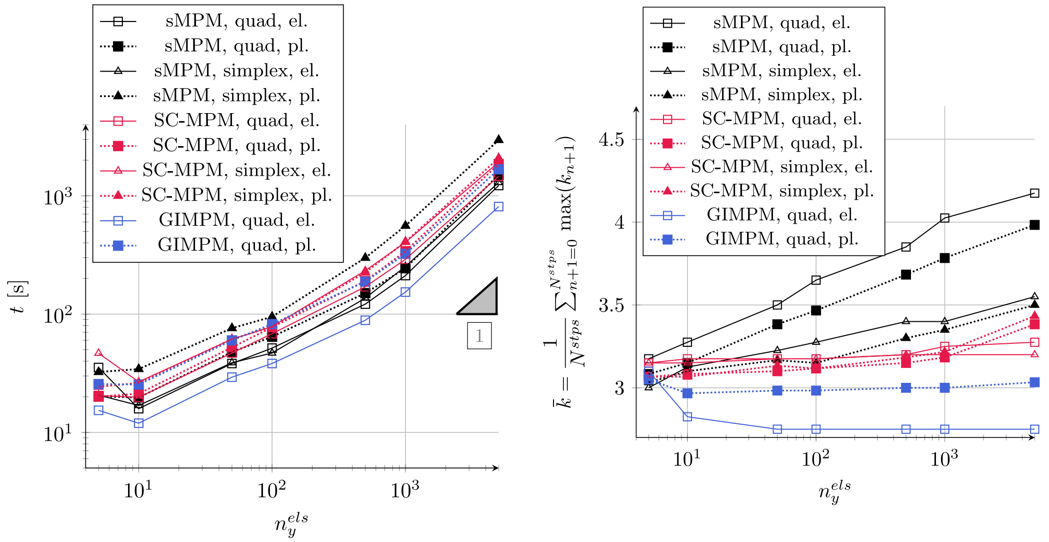

(a) Run times per simulation (log-log scale) for mono-dimensional column under self-weight.

(b) Average NR iterations per simulation (semi-log scale) for mono-dimensional column under self-weight.

**Fig. 12.** Run times (left) and average NR iterations (right) for mono-dimensional column under self-weight. Quad elements for the sMPM, SC-MPM and GIMPM, and simplex elements for the sMPM and SC-MPM are considered for the elastic and elasto-plastic case.

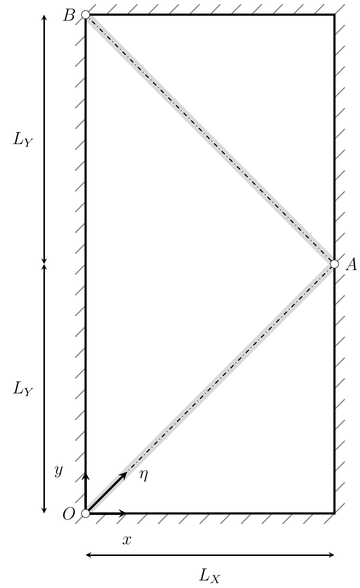

**Fig. 13.** Graphical illustration of the two-dimensional test with MMS.

### 6.2. Two-dimensional test with MMS

*Example scope.* This two-dimensional test uses the Method of Manufactured Solutions (MMS). The desired displacement field is as follows

$$\boldsymbol{u}(\boldsymbol{X}) = \begin{bmatrix} u_x \\ u_y \end{bmatrix} = \begin{bmatrix} a \sin\left(\dfrac{X}{L_X}\pi\right) \sin\left(\dfrac{Y}{L_Y}\dfrac{\pi}{2}\right) \\ 0 \end{bmatrix}, \tag{50}$$

where $a$ describes the amplitude of the displacements and $L_X$ and $L_Y$ are the rectangle lengths reported in Fig. 13.

As standard in the MMS, body forces are computed from the deformation gradient Eq. (1), the elastic logarithmic strains defined in Section 2.1, the adopted elastic constitutive relationship (Eqs. (3) and (5)) and computing the divergence of the Cauchy stress as stated by equilibrium Eq. (2). For the sake of brevity, the computation of the two-dimensional body forces from the given displacements is omitted (see [67] or [68] for procedural details), while their equations are given in the supplementary materials.

This example aims to compare the new SC-MPM with the sMPM and the GIMPM adopting quad and simplex elements. The GIMPM formulation is only considered for quad elements. The sinusoidal displacement field provides a more challenging plane strain solution than that assumed in Section 6.1. Moreover, analytical solutions in terms of any quantities of interest are readily available thanks to the MMS. To exclude possible errors due to the imposition of BCs (especially for the convergence plots), the whole rectangle was modelled despite the symmetry along the horizontal axis.

Similarly to Section 6.1, a set of simulations (labelled $(a)$) is run with the SC-MPM to compare given values of $\beta$ against the adaptive formula Eq. (39). Adopting this adaptive formula for $\beta$, set $(b)$ of simulations is run with different grid refinements for quad elements (employing sMPM, SC-MPM, and GIMPM) and simplex elements (using sMPM and SC-MPM). Errors in displacement and stress fields are compared against the analytical solutions.

*Setup.* All the analyses for this example use a material with the following elastic properties, $E = 1 \times 10^4$ Pa and $\nu = 0.3$ and an initial density of 100 kg m$^{-3}$. The analyses are run in 8 pseudo time-steps, over which the displacement amplitude (denoted $a$ in Eq. (50)) is linearly increased from 0 to its final value of 1 m. All boundary conditions are rollers. The dimensions of the rectangle (see Fig. 13) are $L_X = L_Y = 6$ m. These lengths are subdivided by grid of size $h = \frac{1}{rf}$, which implies $h = h_x = h_y$ for quad elements and a maximum edge size of $h$ allowed by setup for simplex elements. The case of $rf = 1$ is illustrated in Figs. 14 and 15 for quad and simplex elements, respectively. In the case of simulation set $(a)$, $rf$ is set to 5. In the case of simulation set $(b)$, $rf$ takes the following values $[1, 2, 4, 8, 16, 24]$. Since the displacement solution is a sinusoidal function, the number of MPs that initially populate each element is 4 per direction.

Simulation set $(a)$ considers different values of the penalty parameter $\beta$, these being $[0.01, 0.05, 0.1, 0.5, 1, 5]$ m and the adaptive formula Eq. (39). The choice of these values, lower than those considered in Section 6.1, is due to the less constrained nature of this problem. Simulations in the set $(b)$ use the adaptive formula Eq. (39) to test its validity across different grid scales.

In order to compare some quantities of interest for the simulations included in set $(b)$, a diagonal coordinate $\eta$ (see Fig. 13) is introduced that passes through the points $O = (0, 0)$ [m], $A = (6, 6)$ [m] and $B = (0, 12)$ [m]. Given the setup of the simulations, the

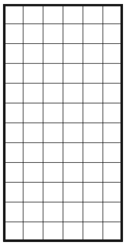

**Fig. 14.** Initial discretisation for quad elements in the case of $rf = 1$, $\sqrt{n^{\text{DoFs}}} \approx 13.49$.

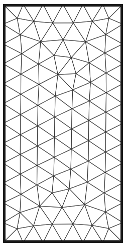

**Fig. 15.** Initial discretisation for simplex elements in the case of $rf = 1$, $\sqrt{n^{\text{DoFs}}} \approx 14.42$.

**Table 3**
Résumé of the error values for the simulations $(a)$ in Fig. 16.

| $\beta$ [m] | $e^{u}$ | $e^{\sigma}$ |
|---|---|---|
| 0.01 | $\approx 3.8 \times 10^{-2}$ | $\approx 6.97 \times 10^{-2}$ |
| 0.05 | $\approx 2.45 \times 10^{-2}$ | $\approx 4.63 \times 10^{-2}$ |
| 0.1 | $\approx 1.68 \times 10^{-2}$ | $\approx 3.42 \times 10^{-2}$ |
| 0.5 | $\approx 8.35 \times 10^{-3}$ | $\approx 2.22 \times 10^{-2}$ |
| 1 | $\approx 1.08 \times 10^{-2}$ | $\approx 3.08 \times 10^{-2}$ |
| 5 | $\approx 3.42 \times 10^{-2}$ | $\approx 9.15 \times 10^{-2}$ |
| Eq. (39) | $\approx 1.19 \times 10^{-2}$ | $\approx 3.32 \times 10^{-2}$ |

MPs will not lie precisely on the axis defined by the coordinate $\eta$. Hence, a bandwidth from the axis $\eta$ (visible in grey in Fig. 13) is defined according to the following formulae

$$\begin{cases} |x^{mp} - y^{mp}| \leq \dfrac{0.2}{rf}; \\ |x^{mp} + y^{mp} - 12| \leq \dfrac{0.2}{rf}. \end{cases} \tag{51}$$

MPs that meet one of the above criteria are included in the plots along the $\eta$ axis. Since this MMS will include a strong component of shear, in the case of GIMPM, the corner update algorithm described in Coombs et al. [37] defines the update of the characteristic length.

The comparison of the runtimes for simulations in the set $(b)$ made use of similar setups to those in Section 6.1 (Hamilton HPC service, MATLAB R2021a running on a Rocky linux 8 and operating on a shared standard node with 32 cores) with the RAM extended to and 256 GB to avoid memory bottlenecks in the analyses.

*Results discussion.* Based on the comparison of the global errors in displacement and stress fields presented in Fig. 16 and Table 3, it is evident that the minimum values occur at a $\beta$ value of 0.5 m for set $(a)$. This value of $\beta$ represents the lowest point of the v-shaped errors in Fig. 16, and, by selecting constant values of $\beta$ progressively further away from 0.5, both error measures increase. Interestingly, the adaptive formula Eq. (39) delivers error values very close to the lowest points of the v-shaped errors, thus further demonstrating its reliability.

Fig. 17 and Table 4 display trends similar to those observed in the mono-dimensional problem 6.1, where the sMPM shows stagnation, while the SC-MPM (for quad and simplex elements) and the GIMPM (for quad elements only) demonstrate convergence. This behaviour is consistent with the global errors in both displacement and stress. Additionally, Fig. 17(a) shows that the sMPM fails with quad elements at $rf = 16$, $\sqrt{\text{nDoFs}} \approx 193.5$. The cause of this failure is also visible in Fig. 20(a), considering $rf = 24$ and $\sqrt{\text{nDoFs}} \approx 289.5$, and is attributed to the emergence of numerical fractures near the $y$-axis. The failure of the sMPM analysis also negatively affects the values of the average slopes and maximum curvatures, which are illustrated in red in Table 4 and should not be taken as indicative. In contrast, neither the SC-MPM nor the GIMPM exhibits this spurious fracture, irrespective of the grid size. The SC-MPM demonstrates approximately linear convergence for both displacements and stresses. The slopes for the stress and the

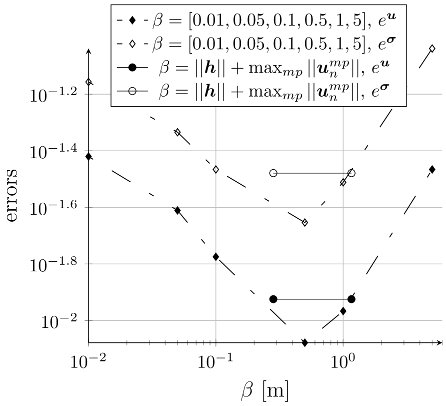

**Fig. 16.** Final global errors of vertical stress for different values of $\beta$ (log-log scale): comparison between assigned values of $\beta$ and adaptive formula from Eq. Eq. (39) for simulations (*a*).

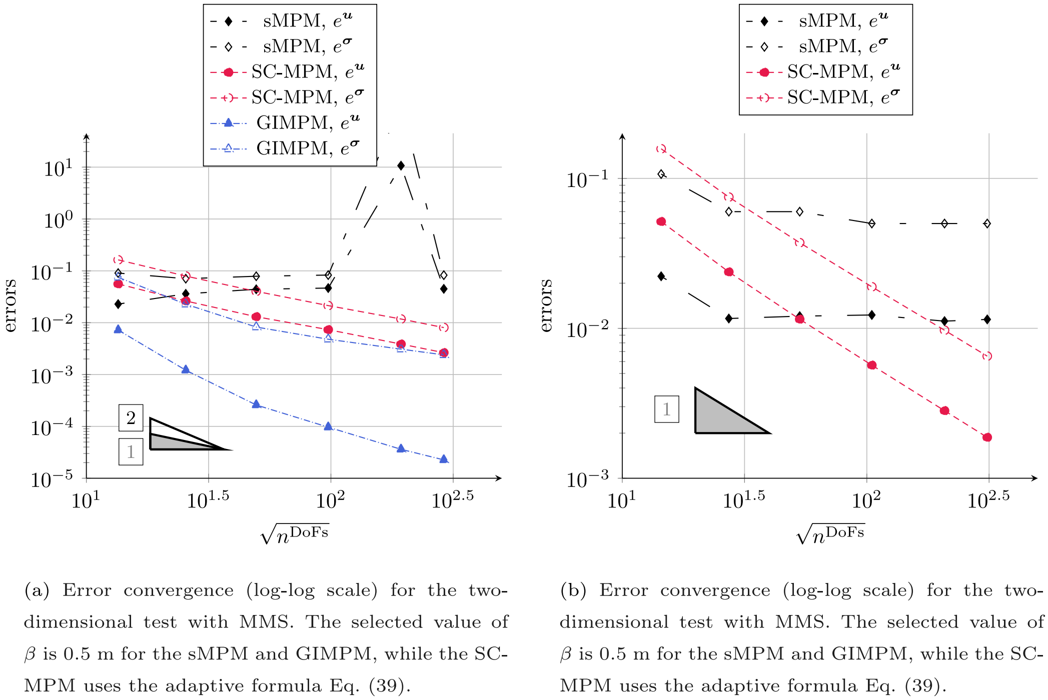

(a) Error convergence (log-log scale) for the two-dimensional test with MMS. The selected value of $\beta$ is 0.5 m for the sMPM and GIMPM, while the SC-MPM uses the adaptive formula Eq. (39).

(b) Error convergence (log-log scale) for the two-dimensional test with MMS. The selected value of $\beta$ is 0.5 m for the sMPM and GIMPM, while the SC-MPM uses the adaptive formula Eq. (39).

**Fig. 17.** Error convergence comparison for quad (left) and simplex (right) elements.

displacements are quite similar, with respective values of $m^{\sigma,\sqrt{n^{\mathrm{DoFs}}}} \approx -0.98$ for quad elements and $m^{\sigma,\sqrt{n^{\mathrm{DoFs}}}} \approx -1.04$ for simplex elements, and $m^{\boldsymbol{u},\sqrt{n^{\mathrm{DoFs}}}} \approx= -0.99$ for quad elements and $m^{\boldsymbol{u},\sqrt{n^{\mathrm{DoFs}}}} \approx= -1.08$ for simplex elements. However, these values are well correlated, as indicated by the very low values of maximum absolute curvature. The GIMPM initially exhibits nearly second-order convergence, transitioning to first-order convergence for the displacement field on finer grids. The stress convergence for the GIMPM follows a similar pattern (i.e., initially closer to second-order behaviour and linear with finer grids), with its average values of slope being $m^{\sigma,\sqrt{n^{\mathrm{DoFs}}}} \approx -1.09$.

Fig. 18 presents the normalised displacement $u_x$ along the normalised axis $\eta$ for the finer grid with $rf = 24$, with $\sqrt{\mathrm{nDoFs}} \approx 289.5$ for quad and $\sqrt{\mathrm{nDoFs}} \approx 310.8$ for simplex elements. Notably, the sMPM results exceed the values predicted by the analytical solution, particularly evident when using quad elements (see Fig. 18(a)). In contrast, there is little discernible difference between the displacements computed using the SC-MPM, GIMPM, and the analytical solution.

Fig. 19 illustrates the normalised values of pressure $p := (\boldsymbol{\sigma} : \mathbf{1})/3$ and shear stress $\sigma_{xy}$ along the normalised axis $\eta$. These are again considered for the finer grid as in the case of Fig. 18. The results indicate that the pressure and shear stress values predicted by the sMPM are spoiled by the cell-crossing instability, which is particularly evident for the shear stresses with simplex elements (see

**Table 4**
Summary of the slopes and maximum curvatures of the trends in Figs. 17(a) (quad elements) and 17(b) (simplex elements) for the two-dimensional test with MMS. Red quantities are reported but must not be considered as significant.

| | | Quad elements | Simplex elements |
|---|---|---|---|
| sMPM | $m^{\boldsymbol{u},\sqrt{n^{\text{DoFs}}}} \approx$ | −0.91 | −0.20 |
| | $\max\left(\lvert\chi^{\boldsymbol{u},\sqrt{n^{\text{DoFs}}}}\rvert\right) \approx$ | 1.02 | 2.41 |
| | $m^{\boldsymbol{\sigma},\sqrt{n^{\text{DoFs}}}} \approx$ | −1.59 | −0.22 |
| | $\max\left(\lvert\chi^{\boldsymbol{\sigma},\sqrt{n^{\text{DoFs}}}}\rvert\right) \approx$ | 1.79 | 2.18 |
| SC-MPM | $m^{\boldsymbol{u},\sqrt{n^{\text{DoFs}}}} \approx$ | −0.99 | −1.08 |
| | $\max\left(\lvert\chi^{\boldsymbol{u},\sqrt{n^{\text{DoFs}}}}\rvert\right) \approx$ | 0.27 | 0.12 |
| | $m^{\boldsymbol{\sigma},\sqrt{n^{\text{DoFs}}}} \approx$ | −0.98 | −1.04 |
| | $\max\left(\lvert\chi^{\boldsymbol{\sigma},\sqrt{n^{\text{DoFs}}}}\rvert\right) \approx$ | 0.13 | 0.12 |
| GIMPM | $m^{\boldsymbol{u},\sqrt{n^{\text{DoFs}}}} \approx$ | −1.84 | – |
| | $\max\left(\lvert\chi^{\boldsymbol{u},\sqrt{n^{\text{DoFs}}}}\rvert\right) \approx$ | 0.31 | – |
| | $m^{\boldsymbol{\sigma},\sqrt{n^{\text{DoFs}}}} \approx$ | −1.09 | – |
| | $\max\left(\lvert\chi^{\boldsymbol{\sigma},\sqrt{n^{\text{DoFs}}}}\rvert\right) \approx$ | 0.70 | – |

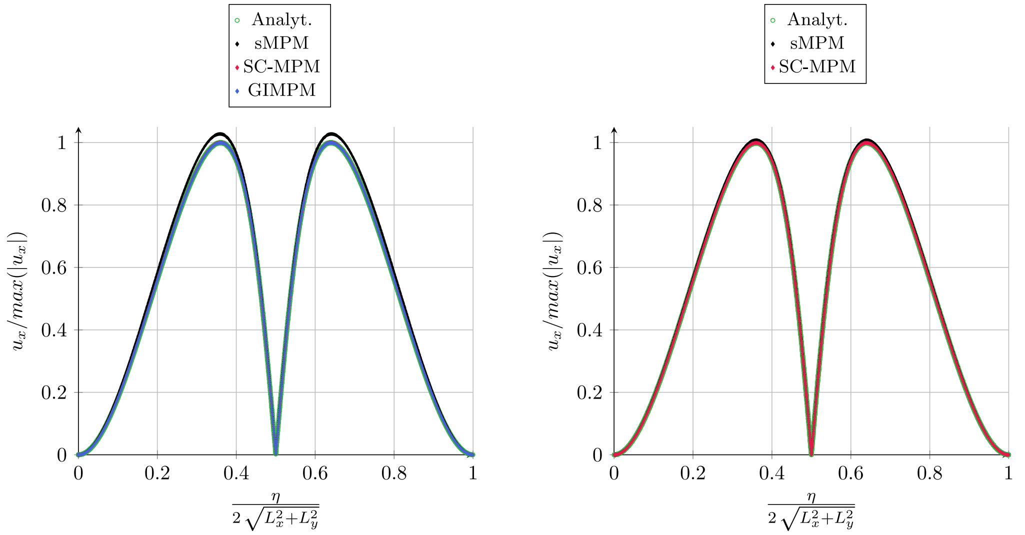

(a) Horizontal displacements along the $\eta$-axis of the two-dimensional MMS test for quad elements.

(b) Horizontal displacements along the $\eta$-axis of the two-dimensional MMS test for simplex elements.

**Fig. 18.** Horizontal displacements for the two-dimensional MMS test for quad (left) and simplex (right). The refinement factor of the grid is $rf = 24$ and the parameter $\beta = 0.5$ m for the sMPM and GIMPM, while the SC-MPM uses the adaptive formula Eq. (39).

Figs. 19(c) and 19(d)). On the other hand, the SC-MPM produces results that are very close to those obtained from both the GIMPM and the analytical solution for quad elements (as shown in Figs. 19(a) and 19(c)) and align closely with the analytical solution for simplex elements (Figs. 19(b) and 19(d)). These findings confirm the effectiveness of SC-MPM in achieving well-behaved stress results, especially when compared to the sMPM, which employs the same shape functions.

Figs. 20 and 21 illustrate the error contours in a logarithmic scale for the displacement (Fig. 20) and stress fields (Fig. 21) for analyses ($b$) with $rf = 24$ ($\sqrt{\text{nDoFs}} \approx 289.5$ for quad elements and $\sqrt{\text{nDoFs}} \approx 310.8$ for simplex elements). Upon initial examination, it is evident that the top rows of Figs. 20 and 21 (obtained with the sMPM) exhibit errors that are several orders of magnitude larger than those in the bottom rows (computed with the SC-MPM). In the case of the displacement field, the maximum errors in Fig. 20(a) are displayed close to the $y$-axis for the sMPM with quad elements. This is because of the artificial numerical fracture mentioned above for this specific set. For the sMPM with simplex elements (Fig. 20(b)), the errors along the $y$-axis persist, but more significant errors are clustered at the corners of the rectangle. These errors are not fully resolved even in the case of SC-MPM (Figs. 20(c) and 20(d)) and are more prominent for the simplex elements (Fig. 20(d)). To understand this behaviour, it is important to note that, although the Dirichlet BCs are conforming and strongly enforced, the MPs close to these boundaries are not free from quadrature errors. The contours of the stress field errors provided by the sMPM (Figs. 21(a) and 21(b)) present a less smooth error distribution than their displacement counterparts, with peaks of red colour rippling the surface. Similar patterns are observed for the SC-MPM (Figs. 21(c) and 21(d)), but the magnitude of errors primarily falls within the blue scale, indicating that they are

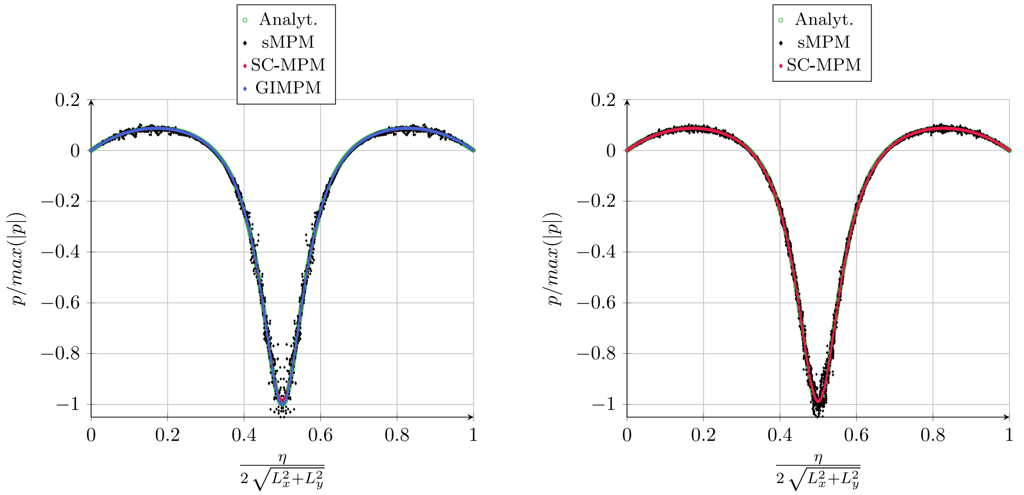

(a) Pressures along the $\eta$-axis of the two-dimensional MMS test for quad elements.

(b) Pressures along the $\eta$-axis of the two-dimensional MMS test for simplex elements.

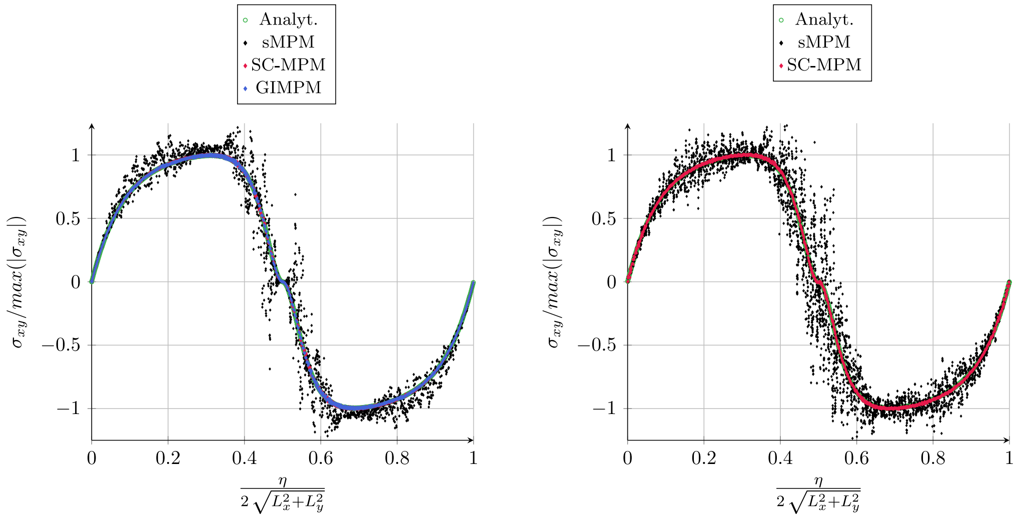

(c) Shear stresses along the $\eta$-axis of the two-dimensional MMS test for quad elements.

(d) Shear stresses along the $\eta$-axis of the two-dimensional MMS test for simplex elements.

**Fig. 19.** Pressures (top row) and shear stresses (bottom row) for the two-dimensional MMS test for quad (left) and simplex (right). The refinement factor of the grid is $a = 24$ and the parameter $\beta = 0.5$ m for the sMPM and GIMPM, while the SC-MPM uses the adaptive formula Eq. (39).

orders of magnitude lower than those produced by the sMPM. Additionally, as demonstrated in Fig. 17 and Table 4, the errors associated with the SC-MPM decrease with grid refinement, justifying the higher computational cost when employing refined grids. The same rationale (i.e., SC-MPM's capacity to mitigate cell-crossing instability) applies to the maximum errors. In the case of quad elements (Figs. 21(a) and 21(c)), the maximum stress error is located midway through the rectangle's height and is more towards the right-hand side. For simplex elements (Figs. 21(b) and 21(d)), the maximum stress error in this region is less pronounced; however, errors at the corners of the rectangle are more significant than those observed with quadrilateral elements.

The comparison of the numerical performances of the sMPM, GIMPM, and SC-MPM is reported in Fig. 22. The exhibited trends are similar to those in Section 6.1, with the simplex elements being more expensive. For these elements, the SC-MPM is slightly more computationally expensive than the sMPM (Fig. 22(a)), despite its average NR iterations being consistently lower (Fig. 22(b)). For the three larger simulations ($rf = 8 - 24$), the SC-MPM is approximately in the range between 13.8% – 14.5% more expensive than the sMPM. The GIMPM appears instead to be the most expensive simulation for quad elements. For this two-dimensional setup, the bandwidth of the tangent matrix is consistently bigger than the mono-dimensional Section 6.1, which motivates the GIMPM slowest performance. The three largest simulations ($rf = 8 - 24$) for the GIMPM and SC-MPM take 31.9% to 43.2% and 13.5% to

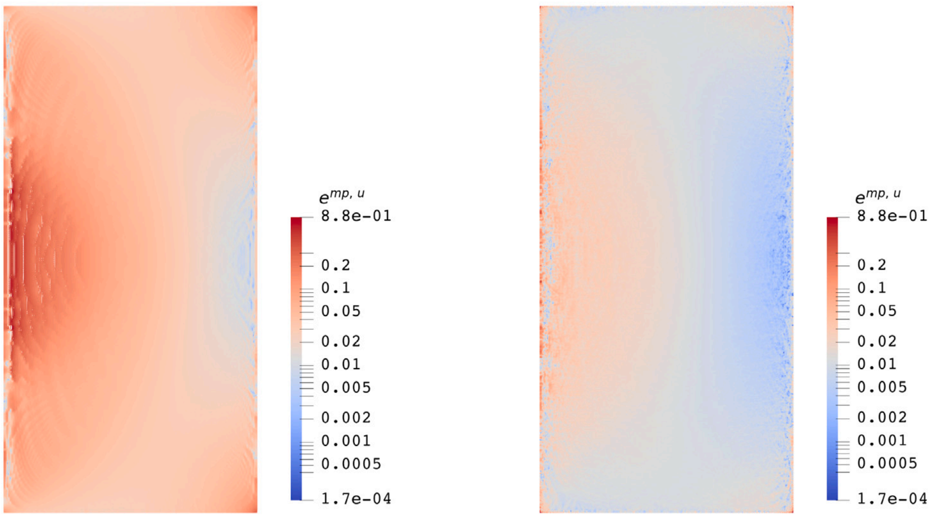

(a) Contours of the displacement error for the sMPM with quad elements.

(b) Contours of the displacement error for the sMPM with simplex elements.

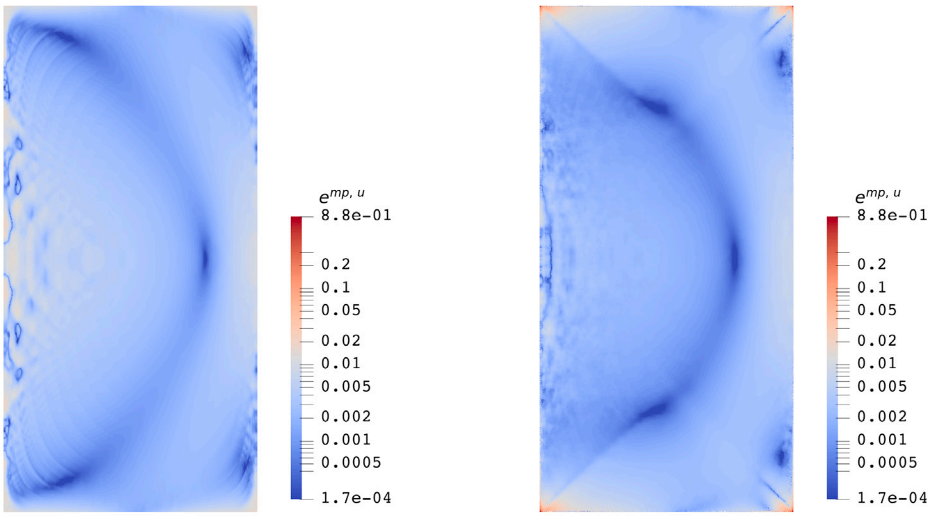

(c) Contours of the displacement error for the SC-MPM with quad elements.

(d) Contours of the displacement error for the SC-MPM with simplex elements.

**Fig. 20.** Contours of the displacement error (logarithmic scale) for the sMPM (top row) and the SC-MPM (bottom row). Quad (left column) and simplex (right column) elements are considered.

17.5% more time, respectively, compared to those with the sMPM. In this context, the SC-MPM proves to be the most cost-effective converging formulation, demonstrating a scaling trend similar to both the GIMPM and sMPM.

### *6.3. Elasto-plastic collapse*

*Example scope.* This numerical example (whose initial setup is illustrated in Fig. 23) has been developed to evaluate the SC-MPM with a more practical scenario, demonstrating extreme displacements and deformations. Additionally, the mapping described in Eq. (43), which involves a strain-like thermodynamic variable, is assessed, as the material under consideration is elasto-plastic with linear isotropic hardening.

*Setup.* The isotropic Hencky material described by Eqs. (3) and (5) has been considered, where the free energy part controlling the isotropic hardening is $\tilde{\Psi}(\alpha) = \frac{1}{2} H \alpha^2$, with $H$ being a constant value. Von Mises plastic yield function similar to that of Section 6.1

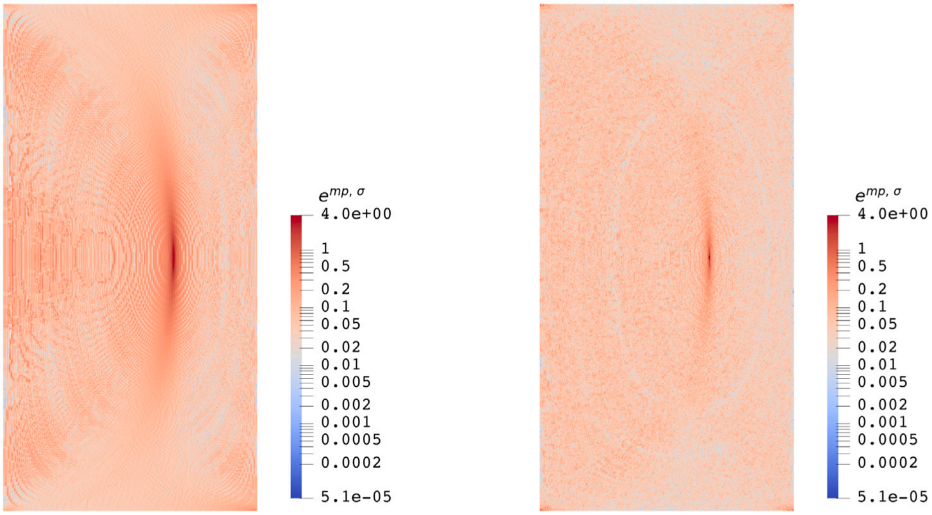

(a) Contours of the stress error for the sMPM with quad elements.

(b) Contours of the stress error for the sMPM with simplex elements.

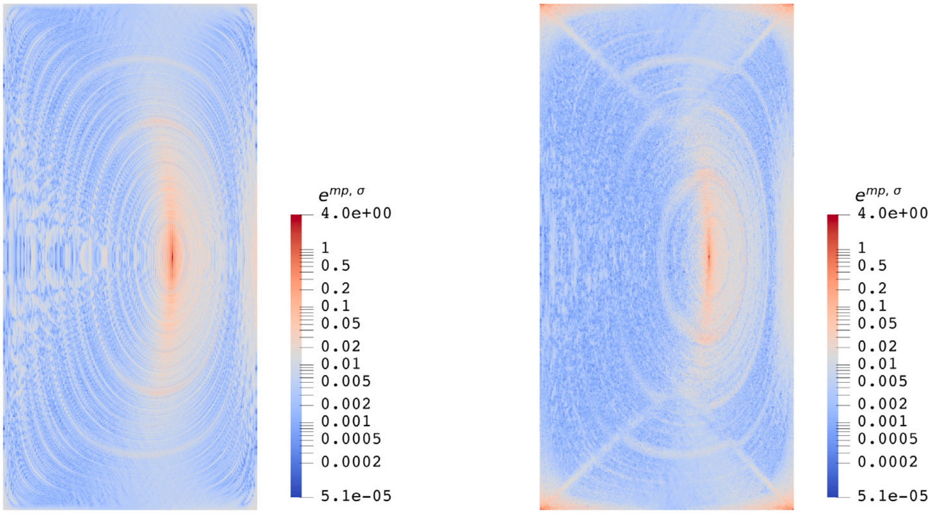

(c) Contours of the stress error for the SC-MPM with quad elements.

(d) Contours of the stress error for the SC-MPM with simplex elements.

**Fig. 21.** Contours of the stress error (logarithmic scale) for the sMPM (top row) and the SC-MPM (bottom row). Quad (left column) and simplex (right column) elements are considered.

has been considered, with the difference of the hardening parameter, i.e.,

$$\boldsymbol{\Phi}\left(\boldsymbol{\tau}, q\right) = \frac{\sqrt{2\, J_2}}{\sigma_y} - \sqrt{\frac{2}{3}}\left(1 - \frac{q}{\sigma_y}\right) = 0, \tag{52}$$

where $q = -\frac{\partial \tilde{\Psi}}{\partial \alpha} = -H\,\alpha$. Specifically, the chosen values of the Young's modulus and Poisson's ratio are $E = 1 \times 10^6$ Pa and $\nu = 0.3$, while the plastic parameters appearing in the yield functions are $\sigma_y = 22 \times 10^3$ Pa and $H = -1 \times 10^3$ Pa. Given the negative value of $H$, it can be seen that softening is introduced. The initial density of the material has been set to ${}^0\rho = 750$ kg m$^{-3}$.

The material, initially occupying the whole height of the simulation (8 m) and one-third of the width (total length of 24 m), is discretised into quad (Fig. 23(a)) and simplex (Fig. 23(b)) elements, with a maximum element size of $1/6$ m. Two MPs per element per direction initially populate each grid element. If the MPs fall beyond the length of 8 m, these are cancelled from the initial setup. This is clearly visible in of Fig. 23(b), where the right-hand side of the homogeneous Neumann boundary is non-conforming from

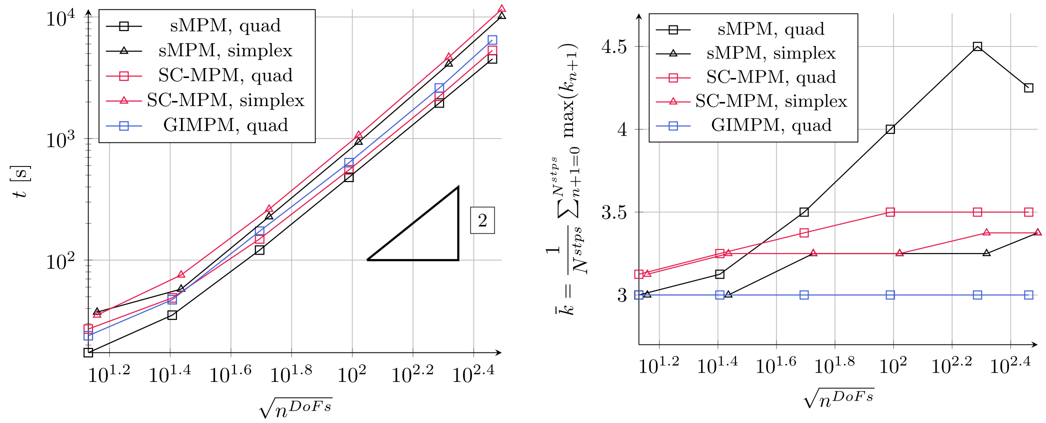

(a) Run times per simulation (log-log scale) for for the two-dimensional MMS test.

(b) Average NR iterations per simulation (semi-log scale) for the two-dimensional MMS test.

**Fig. 22.** Run times (left) and average NR iterations (right) for the two-dimensional MMS test. Quad elements for the sMPM, SC-MPM and GIMPM, and simplex elements for the sMPM and SC-MPM are considered.

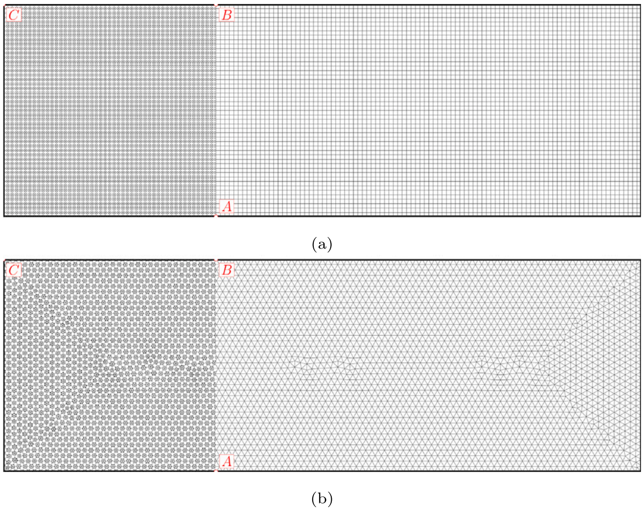

**Fig. 23.** Initial configurations for the elasto-plastic collapse problem for the quad (top) and simplex (bottom) elements.

the beginning of the simulation. The conforming boundaries from point $A$ to $C$ (i.e., bottom and left sides in Fig. 23) are rollers, while the top (from point $C$ to $B$) is homogeneous Neumann.

Three simulations with quad elements (covering sMPM, SC-MPM and GIMPM[12]) and two with simplex elements (including sMPM and SC-MPM) have been run. In all these simulations, the gravitational load is linearly increased with time from 0 to the maximum value of $g = 9.8$ m s$^{-2}$. However, to save computational time, the total pseudo-time of the simulation $T = 100$ s has been divided according into 80 non-equal time-steps according to the following geometric series,

$$T = \sum_{p=0}^{m-1} \Delta t_0 \, c^p \tag{53}$$

where $\Delta t_0 = 2.5$ s, $m - 1 = 80$, and the common ratio has been set to $c \approx 0.979943$. In this way, shorter time-steps are selected towards the end of the simulations, where the material non-linear behaviour and the geometrical non-linearity are combined. For all of these simulations, the penalty parameter has been set according to the adaptive formula Eq. (39).

---

[12] Similarly to Section 6.2, since the simulation is mainly shear dominated, the corner update algorithm described in Coombs et al. [37] is used to update the GIMPM characteristic domain.

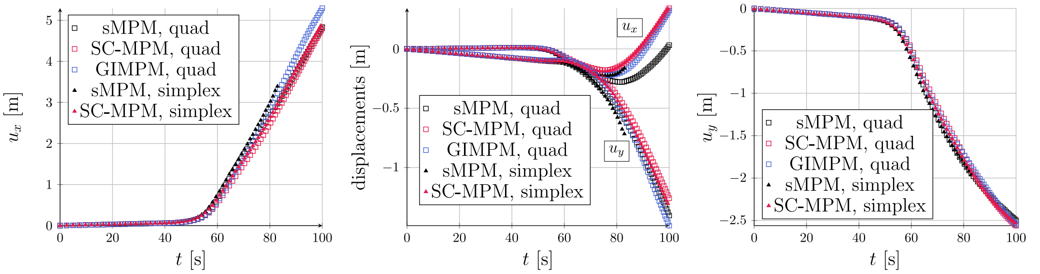

(a) Horizontal displacements of point $A$.

(b) Horizontal and vertical displacements of point $B$.

(c) Vertical displacements of point $C$.

**Fig. 24.** Displacements over pseudo-time at the MPs closest to points $A$ (left figure), $B$ (central figure), and $C$ (right figure) for the different analyses of the elasto-plastic collapse problem.

*Results discussion.* Fig. 24 reports the displacements over time at points $A$, $B$, and $C$ for all the simulations. It can be seen that the simulation employing the sMPM with simplex elements fails in correspondence with the 54nd pseudo-time step. This failure is attributed to a high level of stress oscillation, which, compounded by the nonlinear behaviours, causes the NR solver to fail to converge. Upon closer inspection, it appears that the displacements predicted by the SC-MPM are generally closer to those obtained with the GIMPM than to those calculated with the sMPM. Despite these minor differences, the overall displacement trends are quite similar, as are the deflection shapes at the final time step, which can be seen in the contour plots in Figs. 25–27.

The contours shown in Fig. 25 illustrate the pressure field at the final time step of the completed simulations for four methods: GIMPM with quad elements (Fig. 25(a)), sMPM with quad elements (Fig. 25(b)), SC-MPM (Fig. 25(c)) with quad elements and SC-MPM with simplex elements (Fig. 25(d)). The decision to plot the pressure field stems from the intention to compare the stress components related to the total strain, which is entirely elastic. As observed in the contours, there is very little difference between the GIMPM solution and the SC-MPM results. This further highlights the benefit of the SC-MPM for both quad and simplex elements and proves its advantage over the sMPM, which is plagued by cell-crossing instability.

Similarly, Fig. 26 takes the contours plot of $\sqrt{2\,J_2}$ into account. This time, the goal is to compare the part of the stresses that reach yielding and decrease due to plasticity and softening. From the contours, it is evident that the majority of the slope has reached the yield stress, which has appropriately decreased due to the effects of softening. A few unyielded parts resist in the proximity of point $B$ and its surrounding areas, and a tiny portion close to point $A$. The plots generated by the GIMPM (Fig. 26(a)) and SC-MPM (Figs. 26(c) and 26(d)) are very similar, with only minor differences. However, it is important to compare these contours with those from the sMPM (Fig. 26(b)), which tends to predict spurious, patchy unyielded zones.

For the same reason dealing with the SC-MPM smoothening the displacement and stress field, plastic strains obtained with the GIMPM and the SC-MPM are substantially different. Specifically, the SC-MPM with quad elements (Fig. 27(c)) delivers a smoothened equivalent plastic logarithmic strain, while the same method with the simplex elements (Fig. 27(d)) exhibits very similar contours with though some grid-dependency. On the other hand, the GIMPM (Fig. 27(a)) produces narrower bands of maximum values for $\epsilon_q^p$. However, it also exhibits noisy behaviour in the transitional areas between these bands, particularly noticeable near point $A$ and slightly to its left. In conformity with the stress contour plots in Figs. 25(b) and 26(b), the contours of $\epsilon_q^p$ computed with the sMPM (Fig. 27(b)) suffers from cell-crossing instability. Despite the differences between the SC-MPM and the GIMPM contours of $\epsilon_q^p$, it must be highlighted that the Cauchy continuum with classical elasto-plasticity fails to accurately model strain localisation (see, for instance, Dietsche et al. [69]). Hence, while the SC-MPM and GIMPM results are different, neither represents the physical phenomena with the desired mesh-independent results.

## 7. Conclusions

Table 5 provides a summary of the benefits and weaknesses of the SC-MPM, informed by the theoretical considerations made in Section 4, the outline of the SC-MPM in Section 5 and the numerical comparisons with the sMPM and the GIMPM in Section 6.

Numerical evidence shows that SC-MPM delivers a converging displacement and stress field for quad and simplex elements employing low-order and reduced-stencil shape functions. Furthermore, the SC-MPM provides a stress field free from the cell-crossing instability, which severely inhibits the utility of the sMPM. For quad elements, higher order shape functions have been investigated in the literature to mitigate the cell-crossing, but these come with larger stencils, which blur the body's boundary and trigger even more easily the small-cut issue (unless otherwise addressed, see, e.g., [14,19]). On the other hand, simplex elements have received less attention, and, to the best of the authors' knowledge, no current techniques allow the use of low-order shape functions to generate a cell-crossing-free stress field with these elements. The SC-MPM resolves these issues within a unified framework for the implicit version of the MPM, and maintains runtimes (see Figs. 12(a) and 22(a)) scaling similarly to those of the GIMPM and the sMPM. As indicated above, the SC-MPM technique has the potential to convert an unfitted FEM code that employs linear polynomials into an (oscillation-free) MPM code with only minor modifications. This capability further highlights the connection between the MPM and the family of unfitted FEMs (see to the discussion in [70]).

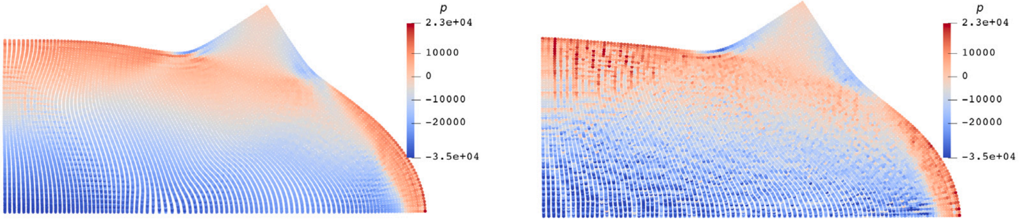

(a) Contours of the pressure field for the GIMPM with quad elements.

(b) Contours of the pressure field for the sMPM with quad elements.

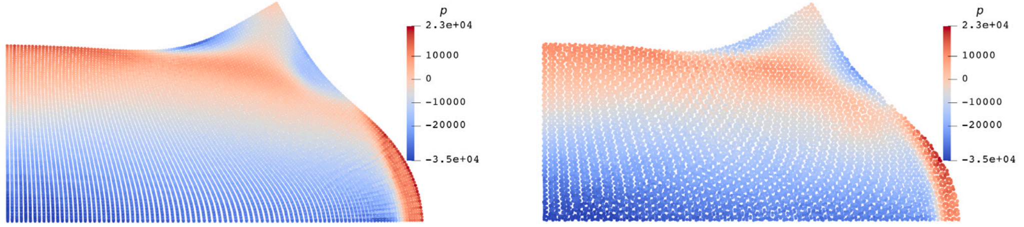

(c) Contours of the pressure field for the SC-MPM with quad elements.

(d) Contours of the pressure field for the SC-MPM with simplex elements.

**Fig. 25.** Contours of the pressure field at the last pseudo time-step for the completed simulations of the elasto-plastic collapse problem.

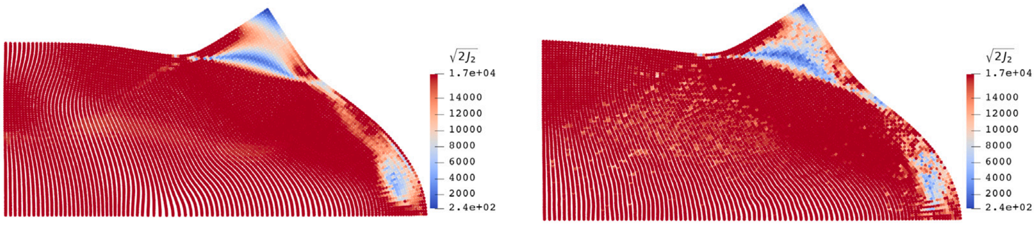

(a) Contours of $\sqrt{2\,J_2}$ for the GIMPM with quad elements.

(b) Contours of $\sqrt{2\,J_2}$ for the sMPM with quad elements.

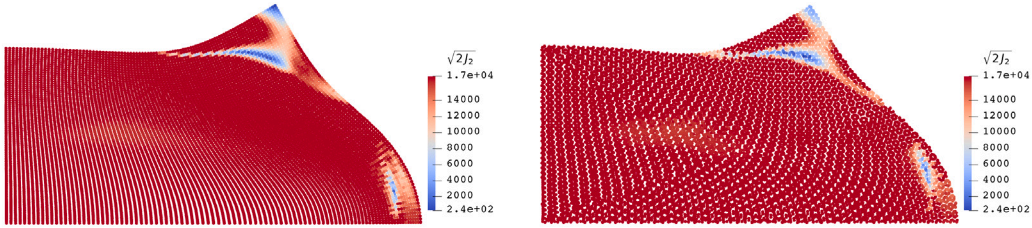

(c) Contours of $\sqrt{2\,J_2}$ for the SC-MPM with quad elements.

(d) Contours of $\sqrt{2\,J_2}$ for the SC-MPM with simplex elements.

**Fig. 26.** Contours of $\sqrt{2\,J_2}$ at the last pseudo time-step for the completed simulations of the elasto-plastic collapse problem.

**Table 5**
Résumé of the advantages and disadvantages of the SC-MPM.

| Advantages | Disadvantages |
|---|---|
| • cell-crossing mitigated & better displacements compared with sMPM<br>• numerical convergence restored for quad and simplex elements<br>• solution is always guaranteed (small-cut issue avoided by default)<br>• reduced stencil for shape functions<br>• competitive runtimes | • mild diffusion of historical variables |

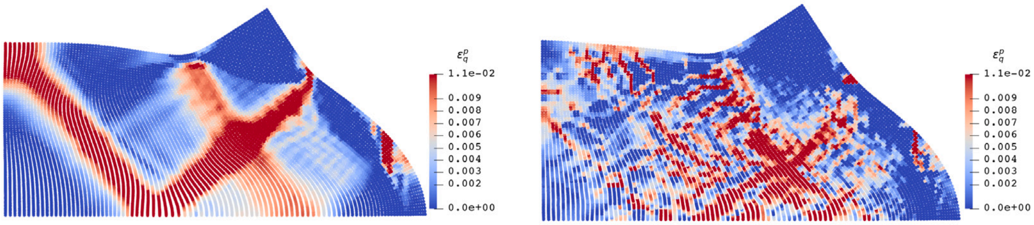

(a) Contours of $\epsilon_q^p$ for the GIMPM with quad elements.

(b) Contours of $\epsilon_q^p$ for the sMPM with quad elements.

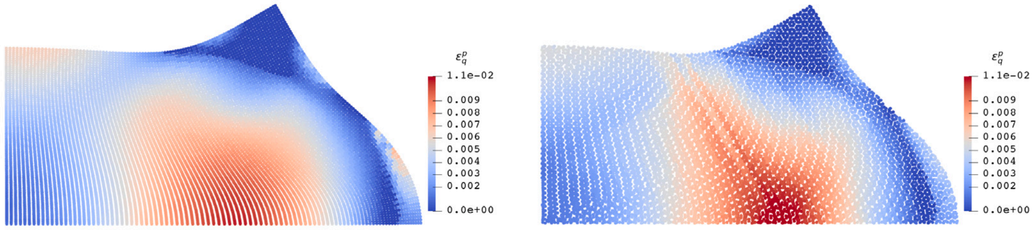

(c) Contours of $\epsilon_q^p$ for the SC-MPM with quad elements.

(d) Contours of $\epsilon_q^p$ for the SC-MPM with simplex elements.

**Fig. 27.** Contours of $\epsilon_q^p$ (equivalent plastic logarithmic strain) at the last pseudo time-step for the completed simulations of the elasto-plastic collapse problem.

However, since the SC-MPM relies on an artificial smoothing and on the mappings Eqs. (40)–(43), this method tends to diffuse the historical variables slightly, thus not capturing the strain localisation phenomena. At the same time, it must be noted that strain localisations are also incorrect in the case of the GIMPM, as it is in the classical theory of elasto-plasticity for the Cauchy continuum (see, in this regard, the references in [71] for materials techniques apt to reproduce localisations). Hence, the implications of reproducing strain localisation with other techniques (e.g., via the Cosserat continuum [71]) still employing the SC-MPM remain an open question that deserves more investigation.

## CRediT authorship contribution statement

**Giuliano Pretti:** Writing – original draft, Visualization, Validation, Software, Methodology, Investigation, Data curation, Conceptualization. **Robert E. Bird:** Writing – review & editing, Conceptualization. **William M. Coombs:** Writing – review & editing, Supervision, Software, Conceptualization. **Charles E. Augarde:** Writing – review & editing, Supervision, Funding acquisition. **Stefano Giani:** Writing – review & editing, Supervision, Methodology, Conceptualization.

## Declaration of competing interest

The authors declare that they have no known competing financial interests or personal relationships that could have appeared to influence the work reported in this paper.

## Acknowledgments

The first author was supported by the Faculty of Science at Durham University, United Kingdom, United Kingdom. The second, fourth and fifth were supported by Engineering and Physical Sciences Research Council, United Kingdom, Grant Number EP/W000970/1. All data created during this research are openly available at http://doi.org/10.15128/r17h149p91f. The research presented in this article has also benefited from discussions with, and feedback from Ted O'Hare, Bradley Sims, Sam Sutcliffe, and Mao Ouyang. For the purpose of open access, the author has applied a Creative Commons Attribution (CC BY) licence to any Author Accepted Manuscript version arising.

## Appendix A. Linearisation of the SC-MPM penalty term

For the sake of linearisation, only the contribution of the additional penalty term in Eq. (35) for the SC-MPM is considered below. Specifically, its contribution relative to a single facet of surface $\gamma_F$ and depending on the nodal displacements of the + and − elements (making the dependencies explicit) can be written in Cartesian components as follows:

$$\mathrm{f}^{pen}_{\mathsf{A}h} := \beta \int_{\gamma_F} \left( \delta_{ih} \left( \frac{\partial \mathrm{N}^+_{\mathsf{A}}\left(\mathbf{u}^+\right)}{\partial x_j} - \frac{\partial \mathrm{N}^-_{\mathsf{A}}\left(\mathbf{u}^-\right)}{\partial x_j} \right) \right) \mathrm{n}^+_j\left(\mathbf{u}^+\right) \left( \sigma^+_{ik}\left(\mathbf{u}^+\right) - \sigma^-_{ik}\left(\mathbf{u}^-\right) \right) \mathrm{n}^+_k\left(\mathbf{u}^+\right) \, \mathrm{d}a\left(\mathbf{u}|_F\right). \tag{A.1}$$

To make the indices of the linearisation clearer, the nodal indices (generically indicated with $\mathsf{A}$) are particularised depending on their belonging to element + or − as follows

- indices $\mathsf{I},\mathsf{H}$ are for the nodes of the + element; and
- indices $\mathsf{J},\mathsf{K}$ are for the nodes of the − element.

In this fashion, the terms in Eq. (A.1) can be divided in the following way

$$\mathrm{f}^{pen}_{\mathsf{A}h} = \mathrm{f}^{++}_{\mathsf{I}h} + \mathrm{f}^{+-}_{\mathsf{I}h} + \mathrm{f}^{-+}_{\mathsf{J}h} + \mathrm{f}^{--}_{\mathsf{J}h}, \tag{A.2}$$

where

$$\mathrm{f}^{++}_{\mathsf{I}h} := \beta \int_{\gamma_F} \left( \delta_{ih} \frac{\partial \mathrm{N}^{+}_{\mathsf{I}}}{\partial x_j} \right) \mathrm{n}^{+}_{j}\, \sigma^{+}_{ik}\, \mathrm{n}^{+}_{k}\, \mathrm{d}a; \tag{A.3}$$

$$\mathrm{f}^{+-}_{\mathsf{I}h} := -\beta \int_{\gamma_F} \left( \delta_{ih} \frac{\partial \mathrm{N}^{+}_{\mathsf{I}}}{\partial x_j} \right) \mathrm{n}^{+}_{j}\, \sigma^{-}_{ik}\, \mathrm{n}^{+}_{k}\, \mathrm{d}a; \tag{A.4}$$

$$\mathrm{f}^{-+}_{\mathsf{J}h} := -\beta \int_{\gamma_F} \left( \delta_{ih} \frac{\partial \mathrm{N}^{-}_{\mathsf{J}}}{\partial x_j} \right) \mathrm{n}^{+}_{j}\, \sigma^{+}_{ik}\, \mathrm{n}^{+}_{k}\, \mathrm{d}a; \tag{A.5}$$

$$\mathrm{f}^{--}_{\mathsf{J}h} := \beta \int_{\gamma_F} \left( \delta_{ih} \frac{\partial \mathrm{N}^{-}_{\mathsf{J}}}{\partial x_j} \right) \mathrm{n}^{+}_{j}\, \sigma^{-}_{ik}\, \mathrm{n}^{+}_{k}\, \mathrm{d}a. \tag{A.6}$$

The current normal to the facet $F$ in the outer direction of the element + is updated as follows:

$$\mathbf{n}^{+} = \frac{\left(\boldsymbol{\Delta F}^{+}\right)^{-T} \cdot \mathbf{n}^{+}_{n}}{\|\left(\boldsymbol{\Delta F}^{+}\right)^{-T} \cdot \mathbf{n}^{+}_{n}\|} \tag{A.7}$$

where $\boldsymbol{\Delta F}^{+} := \boldsymbol{F}^{+} \cdot \left(\boldsymbol{F}^{+}_{n}\right)^{-1}$ and $\mathbf{n}^{+}_{n}$ is the outer normal to the positive facet at the beginning of the step, which is known once the computational grid is introduced. To describe the components of vectors/tensors living in this configuration (i.e., at the beginning of the step), the Cartesian basis vectors $\tilde{\boldsymbol{E}}_{\tilde{I}}$ with $\tilde{I} = 1, \ldots, n^{dim}$ are also introduced. As for those in the original and spatial configuration, all these basis vectors match, i.e., $\boldsymbol{E}_I = \tilde{\boldsymbol{E}}_{\tilde{I}} = \boldsymbol{e}_i$ with $I, \tilde{I}, i = 1, \ldots, n^{dim}$. When the current normal direction is linearised, this gives only a contribution with respect to the nodal displacements of the + element, i.e.,

$$\frac{\partial \mathrm{n}^{+}_{j}}{\partial \mathrm{u}^{+}_{\mathsf{H}p}} = -\mathrm{T}^{n^{+}}_{jq} \frac{\partial \mathrm{N}^{+}_{\mathsf{H}}}{\partial x_q} \delta_{pr}\, \mathrm{n}^{+}_{r}, \tag{A.8}$$

where $\mathbf{T}^{n^{+}} = \mathbf{1} - \mathbf{n}^{+} \otimes \mathbf{n}^{+}$.

Other than the above equations, when linearising with respect to the nodal displacements, the following chain rule is employed

$$\frac{\partial\, (\bullet)^{\pm}}{\partial \mathrm{u}^{\pm}_{\mathsf{A}p}} = \frac{\partial\, (\bullet)^{\pm}}{\partial F^{\pm}_{mN}} \frac{\partial F^{\pm}_{mN}}{\partial \mathrm{u}^{\pm}_{\mathsf{A}p}} = \frac{\partial\, (\bullet)^{\pm}}{\partial F^{\pm}_{mN}} \frac{\partial \mathrm{N}^{\pm}_{\mathsf{A}}}{\partial x_s} F_{sN}\, \delta_{mp}. \tag{A.9}$$

Using the first part of the chain rule on the RHS of the above equation, the following derivatives are calculated as follows

$$\frac{\partial}{\partial F^{\pm}_{mN}} \left( \frac{\partial \mathrm{N}^{\pm}_{\mathsf{A}}}{\partial x_j} \right) = -\frac{\partial \mathrm{N}^{\pm}_{\mathsf{A}}}{\partial X_M} \frac{\partial \left(F^{\pm}\right)^{-1}_{Mj}}{\partial F^{\pm}_{mN}} = -\frac{\partial \mathrm{N}^{\pm}_{\mathsf{A}}}{\partial x_j} \left(F^{\pm}\right)^{-1}_{Nj}; \tag{A.10}$$

$$\frac{\partial}{\partial F^{\pm}_{mN}} \left( \sigma^{\pm}_{ij} \right) = \frac{\partial}{\partial F^{\pm}_{mN}} \left( \frac{1}{J^{\pm}} \tau^{\pm}_{ij} \right) = -\left(F^{\pm}\right)^{-1}_{Nm} \sigma^{\pm}_{ij} + \frac{1}{J^{\pm}} \frac{\partial \tau^{\pm}_{ij}}{\partial F^{\pm}_{mN}}, \tag{A.11}$$

where $\frac{\partial \tau^{\pm}_{ij}}{\partial F^{\pm}_{mN}}$ depends on the material constitutive relationship. Based on Eqs. (A.9) and (A.11), the following quantity is also introduced

$$a^{\pm}_{ijms} := \frac{1}{J^{\pm}} \frac{\partial \tau^{\pm}_{ij}}{\partial F^{\pm}_{mN}} F^{\pm}_{sN} - \sigma^{\pm}_{ij}\, \delta_{ms}. \tag{A.12}$$

Pre-multiplying by $\mathbf{n}^{+}$ the Nanson's formula, the current infinitesimal area can be expressed as a function of the facets' area at the beginning of the step (denoted by $\mathrm{d}a_n$ and with outer normal $\mathbf{n}^{+}_{n}$)

$$\mathrm{d}a = \mathrm{n}^{+}_{j} \left( \mathrm{n}^{+}_{j} \mathrm{d}a \right) = \mathrm{n}^{+}_{j} \left( \Delta J^{+} \left(\Delta F^{+}\right)^{-1}_{j\tilde{M}} \left(\mathrm{n}^{+}_{n}\right)_{\tilde{M}} \right) \mathrm{d}a_n, \tag{A.13}$$

where $\Delta J^{+} = \sqrt{\det(\boldsymbol{\Delta F}^{+} \cdot (\boldsymbol{\Delta F}^{+})^{T})}$. For this case, the derivative with respect to the displacement field gives a contribution only for those nodes belonging to the facet, i.e.,

$$\frac{\partial\, \mathrm{d}a}{\partial \mathrm{u}_{\mathsf{A}p}|_F} = \underbrace{-\,\mathrm{T}^{n^{+}}_{jq} \frac{\partial \mathrm{N}_{\mathsf{A}}|_F}{\partial x_q} \delta_{pr}\, \mathrm{n}^{+}_{r} \left(\mathrm{n}^{+}_{j} \mathrm{d}a\right)}_{=\mathbf{0}} + \mathrm{n}^{+}_{j} \frac{\partial}{\partial \Delta F^{+}_{m\tilde{N}}} \left( \Delta J^{+} \left(\Delta F^{+}\right)^{-1}_{\tilde{M}j} \right) \frac{\partial \mathrm{N}_{\mathsf{A}}|_F}{\partial x_s} \Delta F^{+}_{s\tilde{N}}\, \delta_{mp}\, \mathrm{d}a_n$$

$$= \mathrm{T}^{n^+}_{ms} \frac{\partial \mathrm{N}_{\mathsf{A}}|_F}{\partial x_s} \delta_{mp} \, \mathrm{d}a \tag{A.14}$$

Using the different building blocks Eqs. (A.8)–(A.14), the linearisation of the different components of the SC-MPM penalisation defined by Eqs. (A.3)–(A.6) are as follows

$$\begin{aligned} \frac{\partial \mathrm{f}^{++}_{\mathrm{I}h}}{\partial \mathrm{u}_{\mathsf{A}p}} &= \frac{\partial \mathrm{f}^{++}_{\mathrm{I}h}}{\partial \mathrm{u}^{+}_{\mathsf{H}p}} \\ &= \beta \int_{\gamma_F} \delta_{ih} \frac{\partial \mathrm{N}^{+}_{\mathrm{I}}}{\partial x_j} \left( \left( -\sigma^{+}_{ik}\, \mathrm{n}^{+}_{k}\, \mathrm{n}^{+}_{s}\, \delta_{mj} - \sigma^{+}_{ik}\, \mathrm{n}^{+}_{k}\, \mathrm{T}^{n^+}_{js}\, \mathrm{n}^{+}_{m} + a^{+}_{ikms}\, \mathrm{n}^{+}_{j}\, \mathrm{n}^{+}_{k} - \sigma^{+}_{ik}\, \mathrm{T}^{n^+}_{ks}\, \mathrm{n}^{+}_{j}\, \mathrm{n}^{+}_{m} \right) \frac{\partial \mathrm{N}^{+}_{\mathsf{H}}}{\partial x_s} + \sigma^{+}_{ik}\, \mathrm{n}^{+}_{k}\, \mathrm{n}^{+}_{j}\, \mathrm{T}^{n^+}_{sm} \frac{\partial \mathrm{N}_{\mathsf{A}}|_F}{\partial x_s} \right) \delta_{mp} \, \mathrm{d}a; \end{aligned} \tag{A.15}$$

$$\begin{aligned} \frac{\partial \mathrm{f}^{+-}_{\mathrm{I}h}}{\partial \mathrm{u}_{\mathsf{A}p}} &= \frac{\partial \mathrm{f}^{+-}_{\mathrm{I}h}}{\partial \mathrm{u}^{+}_{\mathsf{H}p}} + \frac{\partial \mathrm{f}^{+-}_{\mathrm{I}h}}{\partial \mathrm{u}^{-}_{\mathsf{K}p}} \\ &= -\beta \int_{\gamma_F} \delta_{ih} \frac{\partial \mathrm{N}^{+}_{\mathrm{I}}}{\partial x_j} \left( \left( -\sigma^{-}_{ik}\, \mathrm{n}^{+}_{k}\, \mathrm{n}^{+}_{s}\, \delta_{mj} - \sigma^{-}_{ik}\, \mathrm{n}^{+}_{k}\, \mathrm{T}^{n^+}_{js}\, \mathrm{n}^{+}_{m} - \sigma^{-}_{ik}\, \mathrm{T}^{n^+}_{ks}\, \mathrm{n}^{+}_{j}\, \mathrm{n}^{+}_{m} \right) \frac{\partial \mathrm{N}^{+}_{\mathsf{H}}}{\partial x_s} + a^{-}_{ikms}\, \mathrm{n}^{+}_{j}\, \mathrm{n}^{+}_{k} \frac{\partial \mathrm{N}^{-}_{\mathsf{K}}}{\partial x_s} + \sigma^{-}_{ik}\, \mathrm{n}^{+}_{k}\, \mathrm{n}^{+}_{j}\, \mathrm{T}^{n^+}_{sm} \frac{\partial \mathrm{N}_{\mathsf{A}}|_F}{\partial x_s} \right) \delta_{mp} \, \mathrm{d}a; \end{aligned} \tag{A.16}$$

$$\begin{aligned} \frac{\partial \mathrm{f}^{-+}_{\mathsf{J}h}}{\partial \mathrm{u}_{\mathsf{A}p}} &= \frac{\partial \mathrm{f}^{-+}_{\mathsf{J}h}}{\partial \mathrm{u}^{+}_{\mathsf{H}p}} + \frac{\partial \mathrm{f}^{-+}_{\mathsf{J}h}}{\partial \mathrm{u}^{-}_{\mathsf{K}p}} \\ &= -\beta \int_{\gamma_F} \delta_{ih} \frac{\partial \mathrm{N}^{-}_{\mathsf{J}}}{\partial x_j} \left( -\sigma^{+}_{ik}\, \mathrm{n}^{+}_{k}\, \mathrm{n}^{+}_{s}\, \delta_{mj} \frac{\partial \mathrm{N}^{-}_{\mathsf{K}}}{\partial x_s} + \left( -\sigma^{+}_{ik}\, \mathrm{n}^{+}_{k}\, \mathrm{T}^{n^+}_{js}\, \mathrm{n}^{+}_{m} + a^{+}_{ikms}\, \mathrm{n}^{+}_{j}\, \mathrm{n}^{+}_{k} - \sigma^{+}_{ik}\, \mathrm{T}^{n^+}_{ks}\, \mathrm{n}^{+}_{j}\, \mathrm{n}^{+}_{m} \right) \frac{\partial \mathrm{N}^{+}_{\mathsf{H}}}{\partial x_s} + \sigma^{+}_{ik}\, \mathrm{n}^{+}_{k}\, \mathrm{n}^{+}_{j}\, \mathrm{T}^{n^+}_{sm} \frac{\partial \mathrm{N}_{\mathsf{A}}|_F}{\partial x_s} \right) \delta_{mp} \, \mathrm{d}a; \end{aligned} \tag{A.17}$$

$$\begin{aligned} \frac{\partial \mathrm{f}^{--}_{\mathsf{J}h}}{\partial \mathrm{u}_{\mathsf{A}p}} &= \frac{\partial \mathrm{f}^{--}_{\mathsf{J}h}}{\partial \mathrm{u}^{+}_{\mathsf{H}p}} + \frac{\partial \mathrm{f}^{--}_{\mathsf{J}h}}{\partial \mathrm{u}^{-}_{\mathsf{K}p}} \\ &= \beta \int_{\gamma_F} \delta_{ih} \frac{\partial \mathrm{N}^{-}_{\mathsf{J}}}{\partial x_j} \left( \left( -\sigma^{-}_{ik}\, \mathrm{n}^{+}_{k}\, \mathrm{n}^{+}_{s}\, \delta_{mj} + a^{-}_{ikms}\, \mathrm{n}^{+}_{j}\, \mathrm{n}^{+}_{k} \right) \frac{\partial \mathrm{N}^{-}_{\mathsf{K}}}{\partial x_s} - \left( \sigma^{+}_{ik}\, \mathrm{n}^{+}_{k}\, \mathrm{T}^{n^+}_{js}\, \mathrm{n}^{+}_{m} + \sigma^{+}_{ik}\, \mathrm{T}^{n^+}_{ks}\, \mathrm{n}^{+}_{j}\, \mathrm{n}^{+}_{m} \right) \frac{\partial \mathrm{N}^{+}_{\mathsf{H}}}{\partial x_s} + \sigma^{-}_{ik}\, \mathrm{n}^{+}_{k}\, \mathrm{n}^{+}_{j}\, \mathrm{T}^{n^+}_{sm} \frac{\partial \mathrm{N}_{\mathsf{A}}|_F}{\partial x_s} \right) \delta_{mp} \, \mathrm{d}a. \end{aligned} \tag{A.18}$$

## Supplementary data

Supplementary material related to this article can be found online at https://doi.org/10.1016/j.cma.2025.118168.

## Data availability

All data created during this research are openly available at http://doi.org/10.15128/r17h149p91f.

## References

[1] D. Sulsky, Z. Chen, H. Schreyer, A particle method for history-dependent materials, Comput. Methods Appl. Mech. Eng. 118 (1–2) (1994) 179–196.

[2] D. Sulsky, S.-J. Zhou, H.L. Schreyer, Application of a particle-in-cell method to solid mechanics, Comput. Phys. Comm. 87 (1–2) (1995) 236–252.

[3] I. Iaconeta, A. Larese, R. Rossi, Z. Guo, Comparison of a Material Point Method and a galerkin meshfree method for the simulation of cohesive-frictional materials, Materials 10 (10) (2017) 1150.

[4] A.A. Madadi, B. Dortdivanlioglu, A subdivision-stabilized B-spline mixed Material Point Method, Comput. Methods Appl. Mech. Engrg. 418 (2024) 116567.

[5] Y. Yokoyama, Y. Kameo, T. Adachi, Development of continuum-based particle models of cell growth and proliferation for simulating tissue morphogenesis, J. Mech. Behav. Biomed. Mater. 142 (2023) 105828.

[6] C. Jiang, C. Schroeder, J. Teran, A. Stomakhin, A. Selle, The Material Point Method for simulating continuum materials, in: Acm Siggraph 2016 Courses, 2016, pp. 1–52.

[7] S.G. Bardenhagen, E.M. Kober, The generalized interpolation Material Point Method, Comput. Model. Eng. Sci. 5 (6) (2004) 477–496.

[8] M. Steffen, R.M. Kirby, M. Berzins, Decoupling and balancing of space and time errors in the material point method (MPM), Internat. J. Numer. Methods Engrg. 82 (10) (2010) 1207–1243.

[9] D. Sulsky, M. Gong, Improving the material-point method, in: Innovative Numerical Approaches for Multi-Field and Multi-Scale Problems: In Honor of Michael Ortiz's 60th Birthday, Springer, 2016, pp. 217–240.

[10] A.S. Baumgarten, K. Kamrin, Analysis and mitigation of spatial integration errors for the material point method, Internat. J. Numer. Methods Engrg. 124 (11) (2023) 2449–2497.

[11] Z. Sun, Y. Gan, J. Tao, Z. Huang, X. Zhou, An improved quadrature scheme in B-spline Material Point Method for large-deformation problem analysis, Eng. Anal. Bound. Elem. 138 (2022) 301–318.

[12] W.M. Coombs, Ghost stabilisation of the Material Point Method for stable quasi-static and dynamic analysis of large deformation problems, Internat. J. Numer. Methods Engrg. 124 (21) (2023) 4841–4875.

[13] G. Pretti, R.E. Bird, N.D. Gavin, W.M. Coombs, C.E. Augarde, A stable poro-mechanical formulation for Material Point Methods leveraging overlapping meshes and multi-field ghost penalisation, Internat. J. Numer. Methods Engrg. 126 (5) (2025) e7630.

[14] Y. Yamaguchi, S. Moriguchi, K. Terada, Extended B-spline-based implicit Material Point Method, Internat. J. Numer. Methods Engrg. 122 (7) (2021) 1746–1769.
[15] E. Burman, Ghost penalty, C. R. Mat. 348 (21–22) (2010) 1217–1220.
[16] K. Höllig, U. Reif, J. Wipper, Weighted extended B-spline approximation of Dirichlet problems, SIAM J. Numer. Anal. 39 (2) (2001) 442–462.
[17] K. Höllig, Finite Element Methods with B-splines, SIAM, 2003.
[18] S. Badia, F. Verdugo, A.F. Martín, The aggregated unfitted finite element method for elliptic problems, Comput. Methods Appl. Mech. Engrg. 336 (2018) 533–553.
[19] W.M. Coombs, R.E. Bird, G. Pretti, The Aggregated Material Point Method (AgMPM), Comput. Methods Appl. Mech. Engrg. 442 (2025) 118012.
[20] Y. Bing, M. Cortis, T. Charlton, W. Coombs, C. Augarde, B-spline based boundary conditions in the Material Point Method, Comput. Struct. 212 (2019) 257–274.
[21] Y. Liang, J. Given, K. Soga, The imposition of nonconforming Neumann boundary condition in the Material Point Method without boundary representation, Comput. Methods Appl. Mech. Engrg. 404 (2023) 115785.
[22] G. Remmerswaal, P.J. Vardon, M.A. Hicks, Inhomogeneous Neumann boundary conditions for MPM and GIMP, Comput. Geotech. 173 (2024) 106494.
[23] N.D. Gavin, G. Pretti, W.M. Coombs, J.C. Brigham, C.E. Augarde, On the implementation of a material point-based arc-length method, Internat. J. Numer. Methods Engrg. (2024) e7438.
[24] M. Cortis, W. Coombs, C. Augarde, M. Brown, A. Brennan, S. Robinson, Imposition of essential boundary conditions in the material point method, Internat. J. Numer. Methods Engrg. 113 (1) (2018) 130–152.
[25] C. Liu, W. Sun, Shift boundary Material Point Method: An image-to-simulation workflow for solids of complex geometries undergoing large deformation, Comput. Part. Mech. 7 (2020) 291–308.
[26] B. Chandra, V. Singer, T. Teschemacher, R. Wüchner, A. Larese, Nonconforming Dirichlet boundary conditions in implicit material point method by means of penalty augmentation, Acta Geotech. 16 (2021) 2315–2335.
[27] V. Singer, T. Teschemacher, A. Larese, R. Wüchner, K.-U. Bletzinger, Lagrange multiplier imposition of non-conforming essential boundary conditions in implicit Material Point Method, Comput. Mech. 73 (2024) 1311–1333.
[28] C. Liu, W. Sun, ILS-MPM: An implicit level-set-based Material Point Method for frictional particulate contact mechanics of deformable particles, Comput. Methods Appl. Mech. Engrg. 369 (2020) 113168.
[29] R.E. Bird, G. Pretti, W.M. Coombs, C.E. Augarde, An implicit material point-to-rigid body contact approach for large deformation soil-structure interaction, Submitt. Comput. Geotech. (2024).
[30] R.E. Bird, G. Pretti, W.M. Coombs, C.E. Augarde, Y.U. Sharif, M.J. Brown, G. Carter, C. Macdonald, K. Johnson, A dynamic implicit 3D material point-to-rigid body contact approach for large deformation analysis, Internat. J. Numer. Methods Engrg. (2025) In press.
[31] Z. Więckowski, The Material Point Method in large strain engineering problems, Comput. Methods Appl. Mech. Engrg. 193 (39–41) (2004) 4417–4438.
[32] L. Beuth, Z. Więckowski, P. Vermeer, Solution of quasi-static large-strain problems by the material point method, Int. J. Numer. Anal. Methods Geomech. 35 (13) (2011) 1451–1465.
[33] I. Jassim, D. Stolle, P. Vermeer, Two-phase dynamic analysis by Material Point Method, Int. J. Numer. Anal. Methods Geomech. 37 (15) (2013) 2502–2522.
[34] P. de Koster, R. Tielen, E. Wobbes, M. Möller, Extension of B-spline Material Point Method for unstructured triangular grids using Powell–Sabin splines, Comput. Part. Mech. 8 (2) (2021) 273–288.
[35] L. Wang, W.M. Coombs, C.E. Augarde, M. Cortis, M.J. Brown, A.J. Brennan, J.A. Knappett, C. Davidson, D. Richards, D.J. White, et al., An efficient and locking-free Material Point Method for three-dimensional analysis with simplex elements, Internat. J. Numer. Methods Engrg. 122 (15) (2021) 3876–3899.
[36] Y. Cao, Y. Zhao, M. Li, Y. Yang, J. Choo, D. Terzopoulos, C. Jiang, Unstructured moving least squares Material Point Methods: a stable kernel approach with continuous gradient reconstruction on general unstructured tessellations, Comput. Mech. (2024) 1–24.
[37] W.M. Coombs, C.E. Augarde, A.J. Brennan, M.J. Brown, T.J. Charlton, J.A. Knappett, Y.G. Motlagh, L. Wang, On Lagrangian mechanics and the implicit Material Point Method for large deformation elasto-plasticity, Comput. Methods Appl. Mech. Engrg. 358 (2020) 112622.
[38] E. Kröner, Allgemeine kontinuumstheorie der versetzungen und eigenspannungen, Arch. Ration. Mech. Anal. 4 (1) (1959) 273–334.
[39] E.H. Lee, Elastic-plastic deformation at finite strains, J. Appl. Mech. 36 (1) (1969) 1–6.
[40] J. Mandel, Plasticité Classique et Viscoplasticité, CISM Courses and Lectures, vol. 97, Springer, 1971.
[41] H. Hencky, The elastic behavior of vulcanized rubber, J. Appl. Mech. (1933).
[42] B. Coleman, W. Noll, The thermodynamics of elastic materials with heat conduction, Arch. Ration. Mech. Anal. 13 (1963) 167.
[43] B.D. Coleman, M.E. Gurtin, Thermodynamics with internal state variables, J. Chem. Phys. 47 (2) (1967) 597–613.
[44] R.v. Mises, Mechanik der plastischen formänderung von kristallen, ZAMM- J. Appl. Math. Mech./ Z. Für Angew. Math. Und Mech. 8 (3) (1928) 161–185.
[45] R. Hill, A variational principle of maximum plastic work in classical plasticity, Quart. J. Mech. Appl. Math. 1 (1) (1948) 18–28.
[46] J.C. Simo, A framework for finite strain elastoplasticity based on maximum plastic dissipation and the multiplicative decomposition: Part I. Continuum formulation, Comput. Methods Appl. Mech. Engrg. 66 (2) (1988) 199–219.
[47] J.C. Simo, A framework for finite strain elastoplasticity based on maximum plastic dissipation and the multiplicative decomposition. Part II: computational aspects, Comput. Methods Appl. Mech. Engrg. 68 (1) (1988) 1–31.
[48] G. Pretti, W.M. Coombs, C.E. Augarde, B. Sims, M.M. Puigvert, J.A.R. Gutiérrez, A conservation law consistent updated Lagrangian Material Point Method for dynamic analysis, J. Comput. Phys. 485 (2023) 112075.
[49] J.E. Guilkey, J.A. Weiss, Implicit time integration for the Material Point Method: Quantitative and algorithmic comparisons with the finite element method, Internat. J. Numer. Methods Engrg. 57 (9) (2003) 1323–1338.
[50] W.M. Coombs, C.E. Augarde, AMPLE: a material point learning environment, Adv. Eng. Softw. 139 (2020) 102748.
[51] T. Charlton, W. Coombs, C. Augarde, IGIMP: An implicit generalised interpolation Material Point Method for large deformations, Comput. Struct. 190 (2017) 108–125.
[52] Y. Gan, Z. Sun, Z. Chen, X. Zhang, Y. Liu, Enhancement of the Material Point Method using B-spline basis functions, Internat. J. Numer. Methods Engrg. 113 (3) (2018) 411–431.
[53] A. Sadeghirad, R.M. Brannon, J. Burghardt, A convected particle domain interpolation technique to extend applicability of the Material Point Method for problems involving massive deformations, Internat. J. Numer. Methods Engrg. 86 (12) (2011) 1435–1456.
[54] A. Sadeghirad, R.M. Brannon, J. Guilkey, Second-order convected particle domain interpolation (CPDI2) with enrichment for weak discontinuities at material interfaces, Internat. J. Numer. Methods Engrg. 95 (11) (2013) 928–952.
[55] D.Z. Zhang, X. Ma, P.T. Giguere, Material Point Method enhanced by modified gradient of shape function, J. Comput. Phys. 230 (16) (2011) 6379–6398.
[56] G. Moutsanidis, C.C. Long, Y. Bazilevs, IGA-MPM: the isogeometric Material Point Method, Comput. Methods Appl. Mech. Engrg. 372 (2020) 113346.
[57] S. Sticko, G. Ludvigsson, G. Kreiss, High-order cut finite elements for the elastic wave equation, Adv. Comput. Math. 46 (3) (2020) 1–28.
[58] H. Liu, L. Zhang, X. Zhang, W. Zheng, Interface-penalty finite element methods for interface problems in H1, H (curl), and H (div), Comput. Methods Appl. Mech. Engrg. 367 (2020) 113137.
[59] S. Badia, E. Neiva, F. Verdugo, Linking ghost penalty and aggregated unfitted methods, Comput. Methods Appl. Mech. Engrg. 388 (2022) 114232.
[60] A. Mota, W. Sun, J.T. Ostien, J.W. Foulk, K.N. Long, Lie-group interpolation and variational recovery for internal variables, Comput. Mech. 52 (2013) 1281–1299.

[61] E. Love, D.L. Sulsky, An unconditionally stable, energy–momentum consistent implementation of the material-point method, Comput. Methods Appl. Mech. Engrg. 195 (33–36) (2006) 3903–3925.

[62] M.G. Duffy, Quadrature over a pyramid or cube of integrands with a singularity at a vertex, SIAM J. Numer. Anal. 19 (6) (1982) 1260–1262.

[63] J.N. Lyness, R. Cools, A Survey of Numerical Cubature Over Triangles, Tech. rep., Argonne National Lab., IL (United States), 1993.

[64] F. Brezzi, J. Pitkäranta, On the stabilization of finite element approximations of the Stokes equations, in: Efficient Solutions of Elliptic Systems: Proceedings of a GAMM-Seminar Kiel, January 27 To 29, 1984, Springer, 1984, pp. 11–19.

[65] D. Boffi, F. Brezzi, M. Fortin, et al., Mixed Finite Element Methods and Applications, Vol. 44, Springer, 2013.

[66] Y. Liang, X. Zhang, Y. Liu, An efficient staggered grid Material Point Method, Comput. Methods Appl. Mech. Engrg. 352 (2019) 85–109.

[67] K. Kamojjala, R. Brannon, A. Sadeghirad, J. Guilkey, Verification tests in solid mechanics, Eng. Comput. 31 (2015) 193–213.

[68] L. Wang, W.M. Coombs, C.E. Augarde, M. Cortis, T. Charlton, M. Brown, J. Knappett, A. Brennan, C. Davidson, D. Richards, et al., On the use of domain-based Material Point Methods for problems involving large distortion, Comput. Methods Appl. Mech. Engrg. 355 (2019) 1003–1025.

[69] A. Dietsche, P. Steinmann, K. Willam, Micropolar elastoplasticity and its role in localization, Int. J. Plast. 9 (7) (1993) 813–831.

[70] W.M. Coombs, G. Pretti, R.E. Bird, Unfitted FEM and MPM: similarities and differences of non-conforming grid-based methods, in: a Festschrift with Springer on the occasion of Prof. Michael Kaliske's 65th birthday next year, in press, 2025.

[71] T.J. O'Hare, P.A. Gourgiotis, W.M. Coombs, C.E. Augarde, An implicit Material Point Method for micropolar solids undergoing large deformations, Comput. Methods Appl. Mech. Engrg. 419 (2024) 116668.